NONLINEAR ANALYSIS OF ELECTRICALLY-COUPLED MICROBEAMS UNDER MECHANICAL SHOCK

by

Moustafa Adel Sayed Ahmed

A Thesis presented to the Faculty of the
American University of Sharjah
College of Engineering
In Partial Fulfillment
of the Requirements
for the Degree of

Master of Science in
Mechanical Engineering

Sharjah, United Arab Emirates

April 2018

© 2018 Moustafa Adel Sayed Ahmed. All rights reserved.

Approval Signatures

We, the undersigned, approve the Master's Thesis of Moustafa Adel Sayed Ahmed.

Thesis Title: Nonlinear Analysis of Electrically-coupled Microbeams under Mechanical Shock

Signature	**Date of Signature** (dd/mm/yyyy)
___________________________	_______________
Dr. Mehdi Ghommem Assistant Professor, Department of Mechanical Engineering Thesis Advisor	
___________________________	_______________
Dr. Samir Emam Associate Professor, Department of Mechanical Engineering Thesis Committee Member	
___________________________	_______________
Dr. Lotfi Romdhane Professor of Mechanical Engineering, Director of Mechatronics Engineering Graduate Program Thesis Committee Member	
___________________________	_______________
Dr. Mamoun Abdel-Hafez Head, Department of Mechanical Engineering	
___________________________	_______________
Dr. Ghaleb Husseini Associate Dean for Graduate Affairs and Research College of Engineering	
___________________________	_______________
Dr. Richard Schoephoerster Dean, College of Engineering	
___________________________	_______________
Dr. Mohamed El-Tarhuni Vice Provost for Graduate Studies	

Acknowledgment

I would like first to thank my Thesis advisor Dr. Mehdi Ghommem in the Mechanical Engineering department at the American University of Sharjah for providing knowledge, guidance, support, and motivation throughout my research stages. The door of Dr. Mehdi Ghommem's office has been always open whenever I have a question about my research. I am deeply beholden for his great assistance, worthy discussion and suggestions.

I would like to thank the American University of Sharjah for granting me a graduate assistantship during my study.

I would like to thank the professors of the Mechanical Engineering Department who taught me the master level courses with mighty teaching methods and skills. I really appreciate their dignified advices and motivation. I would like also to thank Dr. Samir Emam and Dr. Lotfi Romdhane for accepting to serve in my Thesis examining committee and their valuable discussions. My thanks goes to Dr. Abdessattar Abdelkefi from New Mexico State University as well for his comments and suggestions while conducting the work.

Finally, I must express my profound gratitude to my parents for providing me with continuous encouragement throughout my years of study and through the process of researching and writing this Thesis. This accomplishment would not have been possible without them. Thank you.

Abstract

This work presents a theoretical investigation of the dynamic response of electrically-coupled microcantilever beams under the combined effect of squeeze-film damping and mechanical shock for MEMS applications. Several research studies have reported and analyzed the failure of MEMS devices deploying electrically-actuated vibrating beams, such as inertial, bio-mass, and gas sensors, when undergoing mechanical shocks due to the inherent pull-in instability. The sensitivity of the vibrating beams to mechanical shock can also be exploited to design microswitches that are intended to trigger a signal once receiving a mechanical shock to activate safety functionalities, such as airbag systems. We consider two different microsystem designs, namely: single and dual beams, operating at varying conditions. The single-beam system is actuated via a fixed electrode (uncoupled actuation) while the electric actuation of the dual-beam system, comprising two movable microbeams, is achieved by applying a DC and AC voltages among them (coupled actuation). We develop a mathematical model to simulate the dynamic response of the single and dual microbeams while accounting for the Fringing field effect, the squeeze-film damping, and the mechanical shock. The simulation results are in good qualitative and quantitative agreement with those reported in the literature. A parametric study is conducted to investigate the effect of the electric actuation, the initial gap distance, the fluid viscosity, and the beam geometry on the shock response of the microsystem. We observe a significant reduction of 29-36% in the pull-in voltage when considering the dual-beam system in comparison with the single-beam case. The frequency response curves show expanded dynamic pull-in bandwidth when operating the symmetric dual-beam system near the primary resonance. We notice that the dual-beam systems are more robust in terms of resistance to mechanical shock. This shows the suitability of such design for the operation and reliability of MEMS devices in harsh environments characterized by high mechanical shock levels. Breaking the symmetry of the dual beam system in terms of the beams' geometry is found to significantly reduce the resistance to shocks. Given their high sensitivity to mechanical shock, single-beam systems are observed to be more attractive for deployment as microswitches.

Search Terms: ***Nonlinear analysis, electrostatic coupling, mechanical shock, static/dynamic pull-in, fringing-fields, squeeze-film damping***

Table of Contents

Abstract…. 5

List of Figures 7

List of Tables.......... 9

List of Abbreviations 10

Chapter 1. Introduction 11

1.1. Overview 11

1.2. Reliability of MEMS in Shock Environments 12

1.3. Mechanical Shock Detection and Sensing 12

1.4. Threshold Sensors 14

1.5. Squeeze-Film Damping.......... 17

1.6. Fringing Fields Effect 19

1.7. Thesis Objectives 20

1.8. Research Contribution.......... 20

1.9. Thesis Organization 21

Chapter 2. Microsystem Description and Mathematical Model 22

2.1. Microsystem Description 22

2.2. Governing Equations of the Microsystem 23

Chapter 3. Static Analysis of Electrically actuated Microbeams.......... 33

3.1. Static Problem: Solution Approach.......... 33

3.2. Convergence Analysis and Validation.......... 34

3.3. Static Response based on Parallel-plate Model 36

3.4. Static Response: Fringing Field Effect 39

Chapter 4. Dynamic Analysis of Electrically-actuated Microbeams.......... 44

4.1. Natural Frequencies under Electrostatic Forcing.......... 44

4.2. Frequency response: effect of electric actuation and microsystem design 50

Chapter 5. Shock Response of Electrically-actuated Microbeams 56

5.1. Effect of Microsystem Design on the Shock Response 56

5.2. Shock Behavior near Resonance.......... 61

5.3. Effect of Squeeze-film Damping on Shock Response 63

Chapter 6. Conclusion and Future Work 71

References.......... 73

Vita.......... 78

List of Figures

Figure 1.1: LDA curves for initially curved single clamped-clamped microbeam [33]. 14
Figure 1.2: Frequency response of the cantilever microbeams near primary resonance illustrating the concept of STMT (Switch Triggered by Mass Detection). [8] 15
Figure 1.3: A shallow arch undergoing a snap-through motion [13]........ 16
Figure 1.4: 3D view of electrically coupled cantilever microbeams [35]........ 16
Figure 1.5: 3D schematic of parallel-plates sucking and pumping the fluid film [1] 17
Figure 1.6: Illustrative 2D schematic of the electric fields considered in different electrostatic force models [45] 20
Figure 2.1: Schematic of the electrically-actuated microbeams under mechanical shock. 23
Figure 3.1: Static Pull-in convergence 34
Figure 3.2: Static response to DC excitation for case study 1: comparison against numerical results obtained from finite element (FE) model in ANSYS . 35
Figure 3.3: Static response to DC excitation for the different case studies (dual and single beam systems): comparison against previous works. The vertical dashed lines denote the experimental values of the pull-in voltage obtained by Ilyas et al. [34]. 37
Figure 3.4: Variations of the switching time with the DC voltage for the single and dual beam cases. 39
Figure 3.5: Static response to DC excitation for single and dual beams under Parallel plate and Palmer electrostatic models 40
Figure 3.6: Pull-in voltage for different beam widths (Case study 5) 41
Figure 3.7: Pull-in voltage for different gap distances (Case study 5) 43
Figure 4.1: Variations of the natural frequency with the DC voltage for the different case studies (dual and single beam systems): comparison against previous works. Note that the results obtained by Ilyas et al. [34] are originally reported in the nondimensional form 49
Figure 4.2: Effect of fringing fields on the natural frequency of single and dual beams 50
Figure 4.3: Frequency response curves of the microsystem for varying DC and AC voltages for the different case studies (dual and single beam systems). Results are shown near the primary resonance 53
Figure 4.4: Frequency response curves of the microsystem for varying DC and AC voltages for case study 8 (dual beam system). Results are shown near the primary resonance. 54
Figure 5.1: The considered shock function in the dimensionless form 56
Figure 5.2: Variations of the dynamic pull-in voltage with the amplitude of the mechanical shock (case study 1) 57
Figure 5.3: Variations of the dynamic pull-in voltage with the amplitude of the mechanical shock: (a) quasi-static (T = 1 ms) and (b) dynamic loading case (T = 0.1 ms). Results are compared to those reported by Younis et al. [23] 58

Figure 5.4: Variations of the dynamic pull-in voltage with the amplitude of the mechanical shock for different thickness under mechanical shock of 1 ms duration. 59
Figure 5.5: Stable and unstable time history of the microbeam tip: (a) quasi-static (T = 1 ms) and (b) dynamic loading case (T = 0.1 ms). 60
Figure 5.6: Variations of the dynamic pull-in voltage with the amplitude of the mechanical shock for different AC voltages (case study 8). 61
Figure 5.7: Variations of the lowest detectable acceleration (LDA) with the DC voltage for different AC voltages (case study 5): (a) away from the primary resonance, (b) near the primary resonance. 63
Figure 5.8: Time histories of the single beam's tip deflection under 400g shock amplitude. 64
Figure 5.9: Variations of the maximum tip deflection with the effective viscosity when applying a DC voltage of 0.4V and under 400g shock amplitude. (a) Single beam (b) Dual beam (asymmetric) 66
Figure 5.10: Variations of the maximum relative tip deflection of the beams (dual and single beam systems) with the gap distance d under 400g shock amplitude 68
Figure 5.11: Variations of the maximum relative tip deflection of the case study 5 (single beam) with the gap distance d under mechanical shock of amplitude 400g and electrostatic force. 68
Figure 5.12: LDA curves for the single and dual beam under different pressure values 70

List of Tables

Table 2.1: Geometric and material properties of the microbeams under investigation [23, 34] 32
Table 2.2: Case studies under investigation 32
Table 3.1: Static Pull-in voltages obtained for the cases under consideration (coupled and uncoupled actuation): comparison against previous theoretical and experimental studies 38
Table 3.2: Pull-in voltage difference between Parallel-plate and Palmer models of electrostatic force while varying the microbeam width (*b*) 41
Table 3.3: Pull-in voltage difference between Parallel-plate and Palmer models of electrostatic force when varying the gap distance (*d*) 42

List of Abbreviations

MEMS	Micro-electro-mechanical systems
LDA	Least Detectable Acceleration
SQFD	Squeeze-film damping
ROM	Reduced-order model

Chapter 1. Introduction

In this chapter, we provide a brief overview about MEMS applications deploying vibrating microbeams, their associated physical aspects, and the main design requirements. Then, we describe the microsystem investigated in this study as well as the thesis contribution. Finally, the general organization of the thesis is presented.

1.1. Overview

Micro-electro-mechanical systems (MEMS) devices have gained a great focus in the last few decades due to their low cost with the capability to be integrated with electronic circuits and operate with high resolution and low power consumption. MEMS have been widely used for sensing, filtering, and switching applications. Microbeams such as cantilever beams and clamped-clamped beams constitute the basic structure of numerous MEMS devices subjected to different actuation mechanisms including electrostatic, thermal and piezoelectric actuation. Electrostatic actuation is the most common actuation mechanism used given its ease of application and implementation in small spaces and its useful nonlinear features [1]. The design of MEMS devices requires a deep understanding of the nonlinear dynamics associated with vibrating beams. For example, the resulting coupling between the mechanical and electrical components leads to the nonlinear phenomenon named as "pull-in instability". This phenomenon occurs by increasing the voltage to a threshold value where the mechanical restoring force of the beam can no longer balance the electrostatic force resulting in the collapse of the beam into the fixed electrode. The occurrence of pull-in instability is undesired in many applications because it limits the stable operating range. A wide stable range constitute a design requirement in sensing and tuning applications. Moreover, squeeze-film damping (SQFD) is a common dissipation mechanism in MEMS devices, when operating under ambient air pressure, due to the intrinsic design of wide plates separated by small gap distance which allows for better sensing accuracy. Under such conditions, air viscosity and the different pressure distributions form a barrier to the air movement in and out the separation gap that dissipates energy and resists the structure motion. SQFD force is commonly modeled by coupling the Reynold's equation that is derived from Naiver-stokes equation with the vibrating structure governing equations [2].

1.2. Reliability of MEMS in Shock Environments

There is an emerging use of MEMS devices deploying electrically-actuated vibrating beams for several applications including inertial sensors [3-6], bio-mass sensors [7-9], gas sensors [10-12], and RF filters [13-15], thanks to the significant progress in micromachining technology. One important matter that needs to be considered and assessed in the design of these microsystems is their reliability when exposed to mechanical shock and impact during fabrication, shipping, or operation in harsh environments. Numerous research studies have reported failures in the operation of electrically-actuated microbeams when subject to mechanical shock [16-19]. These failures take place through stiction and electric short circuits resulting from the collapse of the vibrating beams and hitting the fixed or movable electrodes. This is associated with the pull-in instability due to the combined effect of the electrostatic forcing and the mechanical shock. The occurrence of pull-in is undesired in many applications because it limits the safe operation range. The presence of mechanical shock can cause an early dynamic pull-in instability due to unexpected dynamic loading and impact imposed on the microbeam structure. As such, the analysis of electrically-actuated beams subject to mechanical shock has gained significant interest in the last few years [20-25] to provide guidance in the design of robust MEMS devices in terms of resistance to mechanical shock or to investigate the possible exploitation of nonlinear phenomena for switching applications.

1.3. Mechanical Shock Detection and Sensing

Many researchers studied the behavior of microbeam systems subject to combination of electrostatic force and mechanical shocks. They showed that these microbeam systems can be used to trigger a signal once receiving a mechanical shock to perform a preventive action [26-29]. These microswitches (or triggers) have gained a major focus since they replaced some complicated sensors while offering smaller size, lower cost, and improved performance. The use of these switches include airbag deployment in automobiles that functions when a sudden change in acceleration occurs. The same concept is exploited to protect electronic devices at free falling by triggering a signal that does an immediate action [23]. The sensors used for the aforementioned applications belong to the category of ”low-g sensors” (g stands for the gravitational constant). Ramini et al. [28] conducted a theoretical investigation of an

electrostatically-actuated resonant switch using a nonlinear single-degree-of-freedom model for earthquake detection. The microsystem was adjusted to operate near the dynamic pull-in bandwidth and being sensitive to low shock levels. Their study was complemented by an experimental investigation to demonstrate the capability of the proposed resonant switch to capture small levels of acceleration in the order of 0.02 g. Jrad et al. [20] proposed a new device comprising an electrostatically actuated cantilever microbeam attached to a tip mass and mounted on top of a compliant board or a printed circuit board. They developed a mathematical model of the proposed design and showed that it provides a great tunability when varying the DC and AC voltages and capability to detect a wide range of acceleration (from 0.33 g to 200 g).

The other shock threshold sensors category is the ”high-g sensors”, which are expected to be sensitive only to high shock levels (the operation range is in the order of thousands of g) and are commonly used in military applications [30-32]. On the other hand, the functionality of many electrically-actuated microsensors can be negatively affected by the mechanical shock [16, 17, 19, 25]. To ensure the reliability of such sensors, mechanical shock effect needs to be avoided by implementing different designs that show more robustness in order to prevent the dynamic pull-in. Wagner et al. [19] performed finite element analysis to optimize the reliability of MEMS accelerometer made of polysilicon cantilever beams with regards to shock loads arising during drop tests. Their optimal design was verified experimentally. Askari and Tahani [24] developed a reduced-order model to analyze the impact of the mechanical shock on the dynamic pull-in instability of electrically-actuated clamped-clamped beams. The shock load is represented by a half-sine waveform with durations varying between 0.1 ms and 1 ms to simulate hard floor drop tests. They observed that setting the shock duration close to the natural period of the microbeam system speeds up the occurrence of the dynamic pull-in.

Ouakad invistigated the reliability of such curved beams when subjected to mechanical shock [33]. Figure 1.1 depicts the snap-through and dynamic pull-in states in two different curves. It was shown that the presence of mechanical shock can cause an early snap-through following a dynamic pull-in if subjected to small shock amplitudes. In addition, Ouakad invistigated the effect of increasing the shallow arch initial curvature which leads to a bi-stable manner.

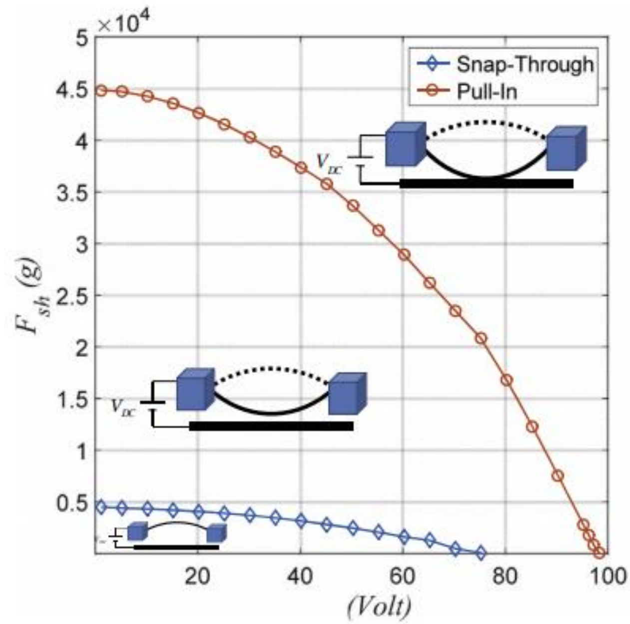

Figure 1.1: LDA curves for initially curved single clamped-clamped microbeam [33].

1.4. Threshold Sensors

Ilyas et al. [34] have recently implemented and tested a new design of a resonator made of a dual electrically-coupled cantilever microbeams. The coupled microsystem showed dynamic features that can be promising in several MEMS applications.

M. Younis et al. [8] studied a method of determining the existence of certain molecules by exploiting the dynamic instabilities of a threshold microswitch. The microswitch can trigger a signal at the existence of a certain mass due to a frequency shift. Clamped-clamped and cantilever beams were tuned to operate near the pull-in band of a predetermined frequency. Figure 1.2 shows the shift in the frequency due to the added mass with the corresponding time histories. It was concluded that tuning the system at twice its primary resonance (subharmonic frequency) produces promising results. At subharmonic frequency the microbeam undergo a sharp transition from the stable (no-mass) to the unstable state (mass detected) [8].

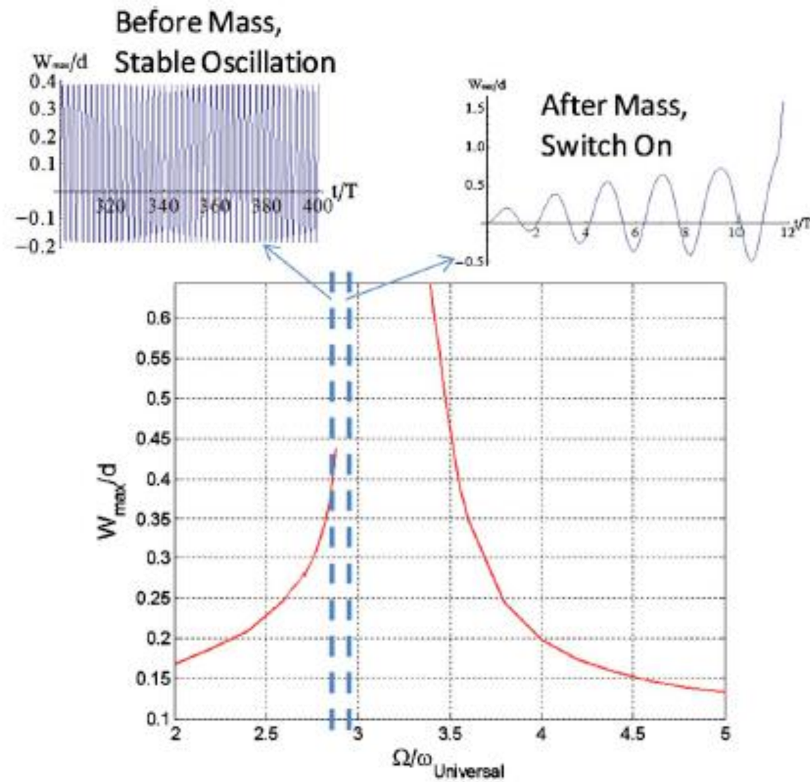

Figure 1.2: Frequency response of the cantilever microbeams near primary resonance illustrating the concept of STMT (Switch Triggered by Mass Detection). [8]

Unlike cantilever beams, clamped-clamped beams have another sort of nonlinearity called "midplane stretching" which is a cubic nonlinearity. Bouchaala et al. [10] also studied the exploitation of dynamic characteristics of the clamped-clamped beam at low and high electrostatic actuation for gas detection. At low electrostatic excitation voltages, midplane stretching nonlinearity becomes dominant and the beam exhibit a hardening behaviour. However, at high actuation voltages, the system shows a softening behaviour. Both nonlinearities were exploited for different purposes in gas detection [10].

Ouakad et al. [13] considered an initially curved microbeams for filtering applications. The arched beam showed promising features, such as interesting jumps and snap-through, when used as band-pass filter. The results showed a sharp roll-off slope and almost a flat bandwidth when exciting near the primary natural frequency, as shown in Figure 1.3 [13].

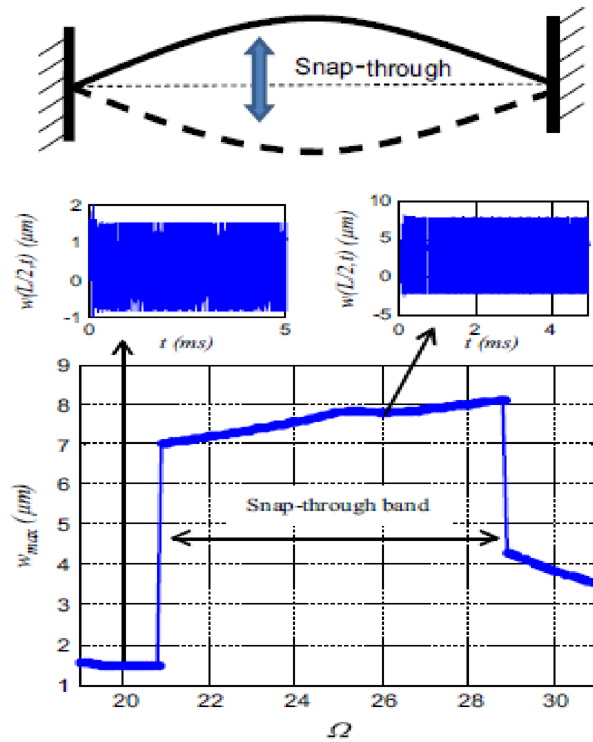

Figure 1.3: A shallow arch undergoing a snap-through motion [13].

Napoli et al. [35] considered the problem of several cantilever microbeams fixed at a common base as shown in Figure 1.4. The closeness of these microbeams affects each other and results in interesting dynamics which was verified experimentally. It was shown that the system can have more than one fundamental natural frequency. An extension to a group of cantilever arrays is also being investigate based on the application of interest [35].

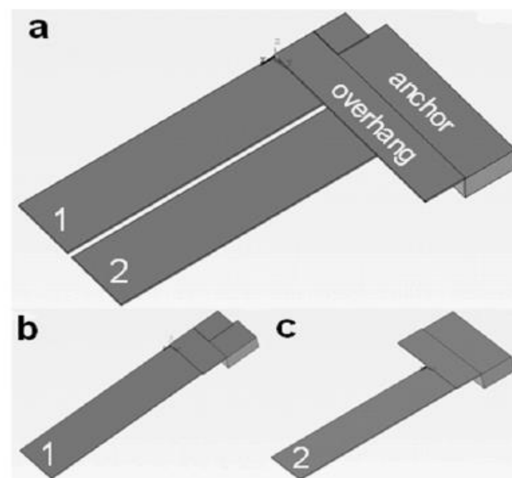

Figure 1.4: 3D view of electrically coupled cantilever microbeams [35]

1.5. Squeeze-Film Damping

In typical MEMS devices, parallel plates with small gap distance is commonly used to achieve higher sensitivity. For such devices, squeeze-film damping (SQFD) force is considered when simulating the dynamic response when operating in ambient air. Extensive research has been conducted to study the pressure distribution between the parallel plates under electrostatic forcing. There are several SQFD models in literature, which can be categorized into two main classes; molecular energy using statistical thermodynamics, and Reynold's equation-based models describing the pressure distribution between the parallel plates. The latter modelling approach has showed better predictability of the experimental results [2]. The Reynold's equation is derived from the Naiver-Stokes and the continuity equations under several assumptions listed below [1]:

- Newtonian Fluid
- The fluid obeys the ideal gas law.
- The variation of pressure along the fluid film is negligible.
- Laminar flow
- Small gap distance between the plates compared to the plate width
- The system is isothermal.
- No-slip condition is assumed (continuum fluid)

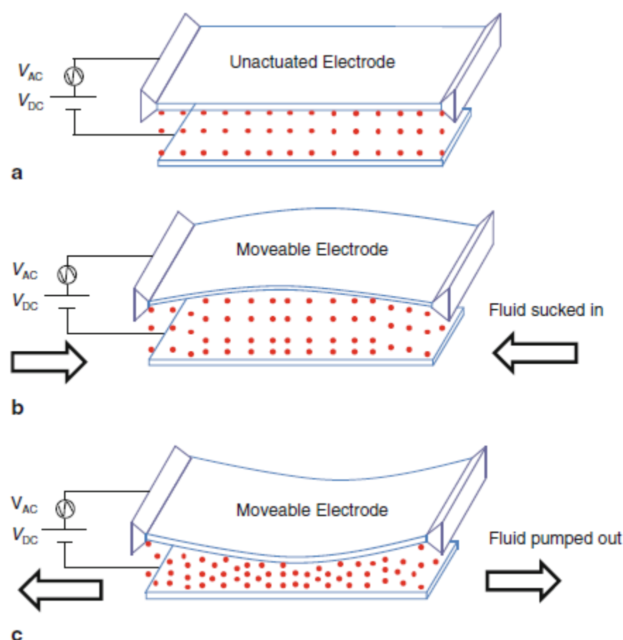

Figure 1.5: 3D schematic of parallel-plates sucking and pumping the fluid film [1]

Starr et al. [36] modelled the squeeze-film damping force of an accelerometer by assuming incompressible fluid film and a small motion of the plates compared to the separation distance. These assumptions reduced the Reynold's equation and made it linear and simple to be solved analytically. Blech et al. [37] solved analytically the compressible linearized Reynold's equation of rigid rectangular and circular parallel plates. He also derived an analytical approximation of the spring damper system between the plates to represent the SQFD force. Nayfeh et al. [2] developed an analytical approximation of the pressure distribution under rectangular and circular plates using perturbation techniques. The analytical equation of the linearized compressible Reynold's equation is then substituted in the main governing equation of the parallel plates and finite element method was used to simulate the dynamic response. They considered varying values of the quality factor for different air pressure values and found a good agreement with the experiments. Following similar approach, Li et al. [38] considered the compressible Reynold's equation to describe the pressure distribution under a cantilever beam. However, they linearized this equation around the ambient pressure and beam static deflection due to DC voltage. He assumed a small oscillation around the static position and hence a small pressure change. Li et al. were successful to simulate the quality factor for different DC voltages and compared their results with their finite element model counterparts based on the software tool ANSYS. They showed significant discrepancy in the quality factor results with previous studies that ignored the static deflection. Hosseini et al. [39] studied the behaviour of initially curved beam operating in different pressure values by solving the full compressible nonlinear Reynold's equation simultaneously with the beam governing equation using finite element method. They showed the effect of SQFD on the dynamic response and concluded that the dependency of the system on ambient air pressure decreases by increasing the length-to-width ratio.

Jordy and Younis [40] investigated the effect of the SQFD and the gap distance on the response of the *g*-sensor subjected to mechanical shock. They claimed that obtaining a higher threshold pull-in voltage can be achieved by decreasing the perforation hole size or the gap distance. This can be beneficial to avoid early dynamic pull-in and stiction to occur by minimizing the hole size. Alsaleem et al. [41] studied the effect of low g-shock effect on the MEMS structure under ambient pressure. They modelled the squeeze-film damping force assuming a linear damping model by using

a constant damping coefficient derived from Blech model. However, the SQFD linear model constitutes a good approximation only for small beam deflection and low pressure values. As such, approaching the substrate under mechanical shock and ambient pressure shows deviations from the actual behaviour of the system. Yagubizade et al. [42] investigated the nonlinear effect of the squeeze-film damping on the clamped-clamped beam system under mechanical shock. They considered the full nonlinear compressible Reynold's equation and solved it simultaneously with the beam's governing equation. It was shown that operating at ambient air pressure decreases significantly the effect of the shock and delays dynamic pull-in occurrence. He concluded that squeeze-film damping force has more effect on the dynamic shock regime than the quasi-static shock regime. Abderezaei et al. [43] considered the incompressible linearized Reynold's equation to model the air pressure under a clamped-clamped beam subjected to mechanical shock while accounting for the Fringing-field effect. They showed a good agreement of the simulation results for moderately small deflection with those obtained by Yagubizade [42] who considered the full nonlinear SQFD model.

1.6. Fringing Fields Effect

The electrostatic force between actuated parallel plates does not result only from the electric fields between the two opposing surfaces. Electric fields are extended some distance away to cover the direction along the width of the plates; this is known as Fringing field effect. This effect should be accounted for as a nonlinear force when the gap distance between the plates (movable or fixed electrodes) is not small relative to the beam width. Several models have been reported in literature, but the most common ones are Palmer model and Meijs-Fokkema model [44].

Figure 1.6 shows the extended electric fields of different fringing-fields models [44]. Batra et al. [44] studied the effect of the Fringing field on cantilever and clamped-clamped microbeams with different thickness-to-width and thickness-to-separation distance ratios. They compared the capacitance per unit length of a suggested empirical formula obtained using the method of moments with different Fringing field models and the Parallel plates model. They claimed that the Fringing field effect is significant when deploying narrow microbeams; that is, small width-to-separation distance ratio,is considered. It was also concluded that several Fringing fields models available in

literature fail to accurately predict the pull-in voltage for microbeams with width smaller than five times the thickness. Ouakad et al. [46] studied the effect of the Fringing field on the static and dynamic response of initially curved clamped-clamped microbeams system. The numerical results were compared with those obtained from the finite element model based on ANSYS and previous experimental studies concluding that Fringing field effect accurately predict the snap-through and pull-in voltages as well as the overall static deflection.

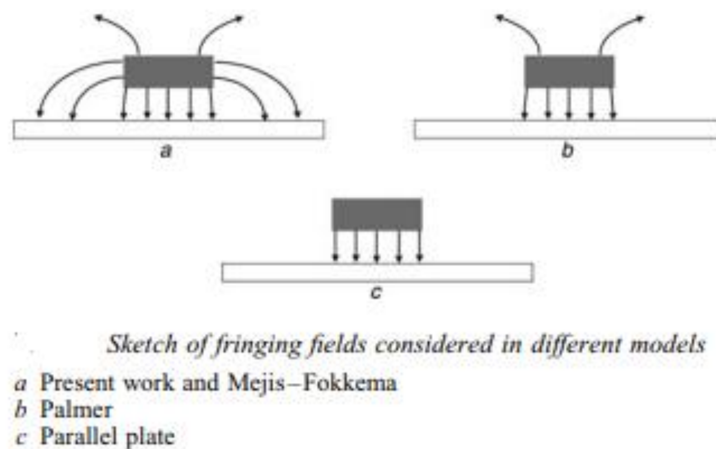

Figure 1.6: Illustrative 2D schematic of the electric fields considered in different electrostatic force models [45]

1.7. Thesis Objectives

Driven by the developing interest in MEMS technology, we perform a non-linear dynamic analysis of micro-cantilever beams under the combination of electric actuation and mechanical shock. To elaborate, we focus on studying the statics and dynamics of a different microbeam structure in comparison with the common single beam case extensively studied in the literature taking into account the Fringing field effect and the nonlinear squeeze-film damping force. The objective of the present study is twofold: (1) to assess the robustness of the microstructure to withstand different levels of shock loads and (2) to investigate the possible use of novel designs for switching applications. A great motivation is that MEMS technology has proven its domination in the market. The rapid increase in the scientific research about MEMS indicates their promising features that can be widely exploited in various fields.

1.8. Research Contribution

The contributions of this research work can be summarized as follows:

- Propose a different microsystem design that consists of a dual movable electrically actuated micro-cantilever beams. Such design results in a robust microsystem in terms of resistance to mechanical shock and therefore greatly delays the occurrence of dynamic pull-in as required in several MEMS applications.
- Study the impact of this design on the system dynamics and the possibility to exploit it in improving some system functionalities.
- Investigate the effect of the Fringing field and SQFD on the proposed microstructure and come up with recommendations to suit different MEMS applications.

1.9. Thesis Organization

The rest of the thesis is organized as follows: Chapter 2 provides the microsystem description and the governing mathematical model. The reduced order model and the numerical techniques are also presented. Chapter 3 deals with the static analysis of different case studies of the microsystem while accounting for the Fringing-field effect. In Chapter 4, we formulate the eigenvalue problem and compute the natural frequencies of the microsystem under electrostatic actuation. We also analyze the frequency response of the microsystem when excited with an AC voltage. Finally, Chapter 5 investigates the dynamic behavior of the microsystem in shock environment under squeeze-film damping effect.

Chapter 2. Microsystem Description and Mathematical Model

In this chapter, we present the problem formulation of the dual beam microsystem that can be used in several MEMS applications as well as stating the governing equations. We also show the development of the reduced order model based on the Galerkin approach.

2.1. Microsystem Description

We consider a MEMS device consisting of two microbeams of different geometry and material properties placed at a gap distance *d* as shown in Figure 2.1. Two fixed electrodes are arranged to be fully exposed to each microbeam (complete overlapping). The separation distance between the upper/lower microbeam and the top/bottom electrode is also *d*. This configuration enables to separately actuate each microbeam by deploying its respective fixed electrode (uncoupled actuation: single beam system) or applying a voltage among the two microbeams while deactivating the fixed electrodes (coupled actuation: dual beam system). We note that the microbeams are selected with different geometry properties to suit various applications. The microsystem is subject to mechanical shock transmitted via the fixed support of the microbeams.

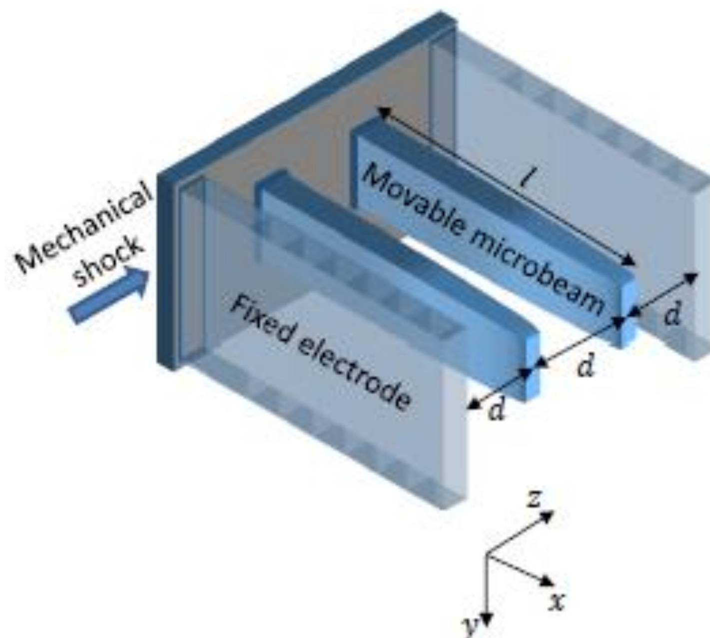

(a) 3D view of the microsystem

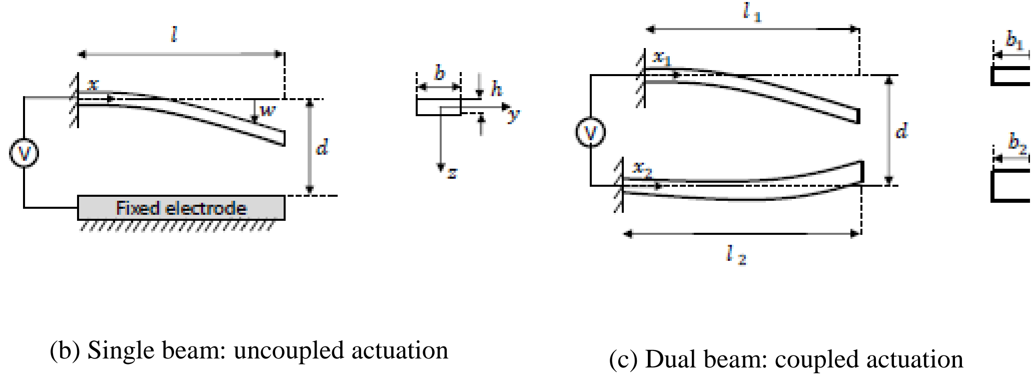

(b) Single beam: uncoupled actuation

(c) Dual beam: coupled actuation

Figure 2.1: Schematic of the electrically-actuated microbeams under mechanical shock.

2.2. Governing Equations of the Microsystem

Based on Euler-Bernoulli beam assumptions, the equations of motion governing the transverse deflections w_i of the electrically-coupled microbeams subject to mechanical shock are given in [34]. We consider the fringing-fields effect, represented in palmer model, and the squeeze film damping effect.

$$\rho b h_1 \ddot{w}_1(x_1,t) + EI_1 w_1''''(x_1,t) = \frac{\varepsilon b\left(V_{DC} + v_{AC}(t)\right)^2}{2\left(d - w_1(x_1,t) + w_2(x_2,t)\right)^2}\left(1 + \frac{\delta\, 0.65}{b}\left(d - w_1(x_1,t) + w_2(x_2,t)\right)\right) + F_{shock} - F_{SQFD} \tag{1}$$

$$\rho b h_2 \ddot{w}_2(x_2,t) + EI_2 w_2''''(x_2,t) = -\frac{\varepsilon b\left(V_{DC} + v_{AC}(t)\right)^2}{2\left(d - w_1(x_1,t) + w_2(x_2,t)\right)^2}\left(1 + \frac{\delta\, 0.65}{b}\left(d - w_1(x_1,t) + w_2(x_2,t)\right)\right) U(x_2 - \xi) + F_{shock} + F_{SQFD} \tag{2}$$

where ρ is the density, b denotes the width of the microbeam, h represents the thickness of the microbeam, E denotes the Young's modulus, I is the beam's cross sectional second moment of area, t is time, and x is the position along the microbeam length. Here, "$'$" denotes the first derivative with respect to x and "$\dot{}$" denotes the time

derivative. The paramete δ is introduced to incorporate the Fringing field effect. Setting $\delta = 0$, electric actuation is represented by the Parallel plates model (neglecting the effect of Fringing field), and for $\delta = 1$, the Palmer model is considered. The parameter $\varepsilon = 8.85X10^{-12}C^2N^{-1}m^{-2}$ is the permittivity of the dielectric vacuum between the movable microbeam and the fixed electrode. V_{DC} and v_{AC} are the DC and AC voltages applied among the microbeams, respectively. The time-varying AC voltage is given by $v_{AC}(t) = V_{AC}\ cos(\Omega_e t)$ where V_{AC} is the voltage magnitude and Ω_e is the excitation frequency. ξ is the gap distance between the two fixed ends of the microbeams, The unit step function U is introduced to account for the discontinuity of the electric field due to the difference in the microbeam lengths.

The shock force per unit length applied on each microbeam is represented by an impact acceleration pulse of a half-sine waveform which is expressed as [16]

$$\mathrm{F_{shock}} = \mathrm{\rho b h_i a_0 g(t)} \tag{3}$$

where a_0 is the amplitude of the shock (given in terms of units of the gravitational constant g). The subscript $i = \{1, 2\}$ refers to microbeam 1 and 2, respectively. The time-varying shock profile $g(t)$ is given by

$$g(t) = sin\left(\frac{\pi t}{T}\right)U(t) + sin\left(\frac{\pi}{T}(t-T)\right)U(t-T) \tag{4}$$

where T denotes the shock duration and $U(t)$ is the unit step function. It should be mentioned that half-sine shock profile is found to approximate well the shape of the actual shock pulse accelerations [16].

F_{SQFD} is the squeeze film damping force applied on both microbeams. We consider Reynold's equation to derive the squeeze film damping force arising from the pressure applied on the microbeam due to the surrounding fluid. Neglecting the body forces and thickness of the fluid film Reynold's equation is given by [1]

$$\frac{\partial}{\partial x}\left(H^3 P\frac{\partial P}{\partial x}\right) + \frac{\partial}{\partial y}\left(H^3 P\frac{\partial P}{\partial y}\right) = 12\,\mu_{eff}\left(H\frac{\partial P}{\partial t} + P\frac{\partial H}{\partial t}\right) \tag{5}$$

where $H = \left(d - w_1(x_1, t) + w_2(x_2, t)\right)$, P is the total pressure of the fluid film, μ_{eff} is the effective viscosity of the surrounding fluid. The boundary conditions at beam edges are

$$P\left(\pm\frac{b}{2}\right) = p_a \tag{6}$$

where p_a is the original static pressure in the gap. The effective viscosity taken equal to the dynamic viscosity of the fluid. We assume incompressible and neglect the time variations of the pressure to simplify the equation and be able to solve it analytically for rectangular beam shapes. In addition, the beam length is considered much larger than the width leading to a significantly higher pressure gradient along the width. Hence, the pressure gradient along the length can be neglected and the equation can be rewritten as

$$\frac{\partial}{\partial y}\left(H^3 P \frac{\partial P}{\partial y}\right) = 12\,\mu\, P\left(\frac{\partial H}{\partial t}\right) \tag{7}$$

where $P = p_a + \Delta p$. Assuming small beam deflection and small pressure gradient by linearizing around the undeflected beam position and static ambient pressure yields [1]

$$\frac{\partial^2 P}{\partial y^2} = -\frac{12\,\mu}{H^3}\left(\frac{\partial w_1}{\partial t} - \frac{\partial w_2}{\partial t}\right) \tag{8}$$

Integrating Equation (8) with the boundary conditions in Equation (6) yields

$$p = \frac{6\,\mu}{H^3}\left(\frac{\partial w_1}{\partial t} - \frac{\partial w_2}{\partial t}\right)\left(\frac{b^2}{4} - y^2\right) \tag{9}$$

The force per unit length F_{SQFD} resulting from the squeeze film damping is obtained by integrating the pressure gradient as

$$F_{SQFD} = \int_{-b/2}^{b/2} \Delta p \, dy$$

$$= \int_{-b/2}^{b/2} \left(\frac{6\,\mu}{H^3} \left(\frac{\partial w_1}{\partial t} - \frac{\partial w_2}{\partial t} \right) \left(\frac{b^2}{4} - y^2 \right) \right) dy$$

$$= \frac{\mu\, b^3}{H^3} \left(\frac{\partial w_1}{\partial t} - \frac{\partial w_2}{\partial t} \right) \tag{10}$$

Substituting Equation (10) in Equations (1) and (2) yields

$$\rho b h_1 \ddot{w}_1(x_1,t) + EI_1 w_1''''(x_1,t) = \frac{\varepsilon b \left(V_{DC} + v_{AC}(t)\right)^2}{2\left(d - w_1(x_1,t) + w_2(x_2,t)\right)^2} \left(1 + \frac{\delta\, 0.65}{b} \left(d - w_1(x_1,t) + w_2(x_2,t)\right) \right) + \rho b h_1 \mathrm{a}_0 g(t) - \mu\, b^3 \frac{\left(\dot{w}_1(x_1,t) - \dot{w}_2(x_2,t)\right)}{\left(d - w_1(x_1,t) + w_2(x_2,t)\right)^3} \tag{11}$$

$$\rho b h_2 \ddot{w}_2(x_2,t) + EI_2 w_2''''(x_2,t) = \frac{-\varepsilon b \left(V_{DC} + v_{AC}(t)\right)^2}{2\left(d - w_1(x_1,t) + w_2(x_2,t)\right)^2} \left(1 + \frac{\delta\, 0.65}{b} \left(d - w_1(x_1,t) + w_2(x_2,t)\right) \right) U(x_2 - \xi) + \rho b h_2 \mathrm{a}_0 g(t) + \mu\, b^3 \frac{\left(\dot{w}_1(x_1,t) - \dot{w}_2(x_2,t)\right)}{\left(d - w_1(x_1,t) + w_2(x_2,t)\right)^3} \tag{12}$$

The boundary conditions of the two cantilever beams are

$$w_{1,2}(0,t) = 0$$

$$\frac{\partial w_{1,2}}{\partial x_{1,2}}(0,t) = 0$$

$$\frac{\partial^2 w_{1,2}}{\partial^2 x_{1,2}}\left(l_{1,2},t\right) = 0$$

$$\frac{\partial^3 w_{1,2}}{\partial^3 x_{1,2}}\left(l_{1,2},t\right) = 0 \tag{13}$$

For convenience, the following non-dimensional variables are introduced

$$\widehat{w}_1 = \frac{w_1}{d}, \hat{x}_1 = \frac{x_1}{l_1}, \widehat{w}_2 = \frac{w_2}{d}, \hat{x}_2 = \frac{x_2}{l_2}, \hat{t} = \frac{t}{\boldsymbol{\tau}}, \hat{T} = \frac{T}{\boldsymbol{\tau}} \tag{14}$$

$$\frac{\rho b h_1 l_1^4}{E I_1 \boldsymbol{\tau}^2} = 1, \boldsymbol{\tau} = \sqrt{\frac{\rho b h_1 l_1^4}{E\, I_1}}, \alpha = \frac{\varepsilon b l_1^4}{2 d^3 E I_1}, \beta = \left(\frac{l_2}{l_1}\right)^4 \left(\frac{h_1}{h_2}\right)^2, \eta = \left(\frac{h_1}{h_2}\right)\beta,$$

$$\lambda = \mathrm{a}_0 \frac{\boldsymbol{\tau}^2}{d}, \kappa = \frac{\mu\, b^3 l_1^4}{E\, I_1 \boldsymbol{\tau}\, d^3} \tag{15}$$

Considering the defined dimensionless form, and dropping the hats, the governing equations can be rewritten

$$\begin{aligned}
&\ddot{\mathrm{w}}_1(\mathrm{x}_1, \mathrm{t}) + \mathrm{w}_1''''(\mathrm{x}_1, \mathrm{t}) \\
&\quad = \alpha \frac{\left(\mathrm{V_{DC}} + \mathrm{v_{AC}}(\mathrm{t})\right)^2}{\left(1 - \mathrm{w}_1(\mathrm{x}_1, \mathrm{t}) + \mathrm{w}_2(\mathrm{x}_2, \mathrm{t})\right)^2} (\left(1. + \frac{\delta\, 0.65\, \mathrm{d}}{\mathrm{b}} \left(1 \right.\right. \\
&\quad \left.\left. - \mathrm{w}_1(\mathrm{x}_1, \mathrm{t}) + \mathrm{w}_2(\mathrm{x}_2, \mathrm{t})\right)\right) + \lambda \mathrm{g}(\mathrm{t}) \\
&\quad - \kappa \frac{\left(\dot{\mathrm{w}}_1(\mathrm{x}_1, \mathrm{t}). - \dot{\mathrm{w}}_2(\mathrm{x}_2, \mathrm{t})\right)}{\left(1 - \mathrm{w}_1(\mathrm{x}_1, \mathrm{t}) + \mathrm{w}_2(\mathrm{x}_2, \mathrm{t})\right)^3}
\end{aligned} \tag{16}$$

$$\begin{aligned}
&\beta \ddot{w}_2(x_2, t) + w_2''''(x_2, t) \\
&\quad = -\eta\alpha \frac{\left(V_{DC} + v_{AC}(t)\right)^2}{\left(1 - w_1(x_1, t) + w_2(x_2, t)\right)^2} \left(1 + \frac{\delta\, 0.65\, d}{b} \left(1 \right.\right. \\
&\quad \left.\left. - w_1(x_1, t) + w_2(x_2, t)\right)\right) U(x_2 - \xi) \\
&\quad + \beta\lambda g(t) + \eta\kappa \frac{\left(\dot{w}_1(x_1, t) - \dot{w}_2(x_2, t)\right)}{\left(1 - w_1(x_1, t) + w_2(x_2, t)\right)^3}
\end{aligned} \tag{17}$$

As for the dimensionless shock profile, it is obtained as

$$g(t) = sin\left(\frac{\pi t}{T}\right) U(t) + sin\left(\frac{\pi}{T}(t - T)\right) U(t - T) \tag{18}$$

The parameter λ presents the magnitude of the shock amplification. Inspecting this parameter, the effect of the mechanical shock of the microsystem dynamics can be amplified by increasing the microbeam length or decreasing its thickness. The parameter β indicates that the difference in the microbeams' thickness introduces asymmetry in the electric actuation and their exposure to the mechanical shock. The thinner microbeam is expected to resist less to the electrostatic force and the mechanical shock.

The normalized boundary conditions are

$$
\begin{aligned}
& w_{1,2}(0,t) = 0 \\
& \frac{\partial w_{1,2}}{\partial x_{1,2}}(0,t) = 0 \\
& \frac{\partial^2 w_{1,2}}{\partial^2 x_{1,2}}(1,t) = 0 \\
& \frac{\partial^3 w_{1,2}}{\partial^3 x_{1,2}}(1,t) = 0
\end{aligned}
\tag{19}
$$

To analyze the impact of different forms of damping, we first neglect the squeeze-film damping force to simulate the system dynamics near vacuum condition. Towards this, we consider a linear damping term $c\, \dot{w}_{1,2}(x_{1,2}, t)$ added to the governing Equations (1) and (2) where the damping coefficient is given by $= \frac{\omega}{Q}$, ω is the natural frequency and Q is the quality factor. Setting high value to Q will be representative of the near vacuum conditions.

2.3. Procedure and Reduced-order Model

To examine the dynamics of the electrically-coupled microbeams under mechanical shock, we derive the reduced-order model (ROM) using the Galerkin method. This method transforms the governing equations and boundary conditions given by Equations (16)-(18) into a set of ordinary differential equations, which simulate the beam deflection. The deflections of the microbeams are expanded as [1]

$$\widehat{w}_1(x_1,t) = \sum_{i=1}^{n} u_i(t)\emptyset_i(x_1) \tag{20}$$

$$\widehat{w}_2(x_2,t) = \sum_{i=1}^{n} v_i(t)\emptyset_i(x_2) \tag{21}$$

where $u_i(t)$ and $v_i(t)$ are generalized coordinates to be solved for. $\emptyset_i(x)$ is the ith modeshape of the cantilever beam.

Next, we substitute Equations (20) and (21) into Equations (16) and (17), multiply the outcome by the mode shape $\emptyset_i(x)$, and integrate the resulting equations over the domain from 0 to 1 to obtain the ROM given by

$$\int_0^1 \emptyset_j(x_1)\left(\sum_{i=1}^{n} u_i(t)\emptyset_i''''(x_1) + \sum_{i=1}^{n} \ddot{u}_i(t)\emptyset_i(x_1)\right)dx_1$$
$$= \alpha\left(V_{DC}+v_{AC}(t)\right)^2 \int_0^1 \left(\frac{\emptyset_j(x_1)}{(1-\sum_{i=1}^{n} u_i(t)\emptyset_i(x_1)+\sum_{i=1}^{n} v_i(t)\emptyset_i(x_2)\ )^2}\right)\left(1\right.$$
$$\left.+\frac{\delta\ 0.65\ d}{b}\left(1-\sum_{i=1}^{n} u_i(t)\emptyset_i(x_1)+\sum_{i=1}^{n} v_i(t)\emptyset_i(x_2)\right)\right)dx_1$$
$$+\lambda g(t)\int_0^1 \emptyset_j(x_1)\ dx_1$$
$$-\kappa\int_0^1 \emptyset_j(x_1)\ \frac{(\sum_{i=1}^{n} \dot{u}_i(t)\emptyset_i(x_1)-\sum_{i=1}^{n} \dot{v}_i(t)\emptyset_i(x_2))}{(1-\sum_{i=1}^{n} u_i(t)\emptyset_i(x_1)+\sum_{i=1}^{n} v_i(t)\emptyset_i(x_2)\ )^3}dx_1 \qquad (22)$$

$$\int_0^1 \emptyset_j(x_2)\left(\sum_{i=1}^{n} v_i(t)\emptyset_i''''(x_2)\ (+\beta\sum_{i=1}^{n} \ddot{v}_i(t)\emptyset_i(x_2)\right)dx_2$$
$$= -\eta\alpha\left(V_{DC}.+v_{AC}(t)\right)^2 \int_0^1 \left(\frac{\emptyset_j(x_2)}{(1-\sum_{i=1}^{n} u_i(t)\emptyset_i(x_1)+\sum_{i=1}^{n} v_i(t)\emptyset_i(x_2)\ )^2}\right)$$
$$-\left(1+\frac{\delta\ 0.65\ d}{b}\left(1-\sum_{i=1}^{n} u_i(t)\emptyset_i(x_1)+\sum_{i=1}^{n} v_i(t)\emptyset_i(x_2)\right)\right)U(x_2-\xi)dx_2$$
$$+\beta\lambda g(t)\int_0^1 \emptyset_j(x_2)\ dx_2$$
$$+\eta\kappa\int_0^1 \emptyset_j(x_2)\frac{(\sum_{i=1}^{n} \dot{u}_i(t)\emptyset_i(x_1)-\sum_{i=1}^{n} \dot{v}_i(t)\emptyset_i(x_2))}{(1-\sum_{i=1}^{n} u_i(t)\emptyset_i(x_1)+\sum_{i=1}^{n} v_i(t)\emptyset_i(x_2)\ )^3}dx_2 \qquad (23)$$

In order to simplify the Equations (22) and (23) and solve them numerically, we multiply both sides of the equations by their denominators to obtain the following system of equations

$$\int_0^1 \emptyset_j(x_1)\left(\sum_{i=1}^{n} u_i(t)\emptyset_i''''(x_1) + \sum_{i=1}^{n} \ddot{u}_i(t)\emptyset_i(x_1)\right)\left(1 - \sum_{i=1}^{n} u_i(t)\emptyset_i(x_1) + \sum_{i=1}^{n} v_i(t)\emptyset_i(x_2)\right)^3 dx_1$$

$$= \alpha\big(V_{DC} + v_{AC}(t)\big)^2 \int_0^1 \emptyset_j(x_1)\left(1 + \frac{\delta\, 0.65\, d}{b}\left(1 - \sum_{i=1}^{n} u_i(t)\emptyset_i(x_1) + \sum_{i=1}^{n} v_i(t)\emptyset_i(x_2)\right)\right)\left(1 - \sum_{i=1}^{n} u_i(t)\emptyset_i(x_1) + \sum_{i=1}^{n} v_i(t)\emptyset_i(x_2)\right) dx_1$$

$$+ \lambda g(t) \int_0^1 \emptyset_j(x_1)\left(1 - \sum_{i=1}^{n} u_i(t)\emptyset_i(x_1) + \sum_{i=1}^{n} v_i(t)\emptyset_i(x_2)\right)^3 dx_1$$

$$- \kappa \int_0^1 \emptyset_j(x_1)\left(\sum_{i=1}^{n} \dot{u}_i(t)\emptyset_i(x_1) - \sum_{i=1}^{n} \dot{v}_i(t)\emptyset_i(x_2)\right) dx_1 \qquad (24)$$

$$\int_0^1 \emptyset_j(x_2)\left(\sum_{i=1}^{n} v_i(t)\emptyset_i''''(x_2) + \beta\sum_{i=1}^{n} \ddot{v}_i(t)\emptyset_i(x_2)\right)\left(1 - \sum_{i=1}^{n} u_i(t)\emptyset_i(x_1) + \sum_{i=1}^{n} v_i(t)\emptyset_i(x_2)\right)^3 \mathrm{d}x_2$$

$$= -\eta\alpha\left(\mathrm{V_{DC}} + v_{\mathrm{AC}}(t)\right)^2 \int_0^1 \emptyset_j(x_2)\left(1 + \frac{\delta\, 0.65\, d}{b}\left(1 - \sum_{i=1}^{n} u_i(t)\emptyset_i(x_1) + \sum_{i=1}^{n} v_i(t)\emptyset_i(x_2)\right)\right)\left(1 - \sum_{i=1}^{n} u_i(t)\emptyset_i(x_1) + \sum_{i=1}^{n} v_i(t)\emptyset_i(x_2)\right) U(\mathrm{x}_2 - \xi)\, \mathrm{d}x_2$$

$$+ \beta\lambda g(t) \int_0^1 \emptyset_j(x_2)\left(1 - \sum_{i=1}^{n} u_i(t)\emptyset_i(x_1) + \sum_{i=1}^{n} v_i(t)\emptyset_i(x_2)\right)^3 \mathrm{d}x_2$$

$$+ \eta\kappa \int_0^1 \emptyset_j(x_2)\left(\sum_{i=1}^{n} \dot{u}_i(t)\emptyset_i(x_1) - \sum_{i=1}^{n} \dot{v}_i(t)\emptyset_i(x_2)\right) \mathrm{d}x_2 \qquad (25)$$

The obtained system of ordinary differential equations are numerically integrated using the Runge-Kutta method to simulate the dynamic response of the microsystem.

In the present study, we consider microbeams of different geometric and material properties to investigate the static and dynamic behavior under varying operating conditions (electric actuation and mechanical shock). The objective is to analyze numerically various microsystem designs so that the switches resulting from the pull-in instability can be activated at different shock levels based on the application of interest. The geometric and material properties of the microbeams under consideration are presented in Table 2.1. The case studies of electrically actuated microbeams are summarized in Table 2.2. Some of these cases are selected to verify the predictive capability of the developed ROM.

Table 2.1: Geometric and material properties of the microbeams under investigation [23, 34]

Reference	l (μm)	b (μm)	h (μm)	d (μm)	E (GPa)	ρ (kg/m^3)
Microbeam1	100	25	3	2	184	2300
Microbeam2	105	25	3	2	184	2300
Microbeam3	100	10	0.1	2	169	2300
Microbeam4	100	10	0.2	2	169	2300

Table 2.2: Case studies under investigation

Case study	Electric actuation	Microbeam(s)
Case study 1	Uncoupled	Microbeam1
Case study 2	Uncoupled	Microbeam2
Case study 3	Coupled	Microbeam1- Microbeam1
Case study 4	Coupled	Microbeam1- Microbeam2
Case study 5	Uncoupled	Microbeam3
Case study 6	Uncoupled	Microbeam4
Case study 7	Coupled	Microbeam3- Microbeam3
Case study 8	Coupled	Microbeam3- Microbeam4

Chapter 3. Static Analysis of Electrically actuated Microbeams

In this chapter, we present the simulation results obtained for the static response of the electrically actuated cantilever microbeams. We evaluate the static performance of the mentioned case studies while using two electrostatic forcing models, namely Parallel-plates model and Palmer model.

3.1. Static Problem: Solution Approach

The microsystem is actuated by applying the electrostatic forcing and then we first analyze the static response and identify the critical DC voltage that leads to the pull-in instability onset; that is, the upper limit of the electrical potential at which the balance between the structural restoring force and electrostatic force is destroyed and the microbeam system collapses. We note that for the static analysis to analyze the pull-in instability, the time-dependent terms arising from the inertia, the damping, the electric actuation (AC voltage), and the shock pulse acceleration in the ROM given by Equations (24) and (25) are cancelled while substituting the time-varying modal coordinates $u_i(t)$ and $v_i(t)$ by unknown constants C_i and D_i. We obtain instead the following system of nonlinear algebraic equations:

$$\int_0^1 \emptyset_j(x_1)\left(\sum_{i=1}^{n} C_i\, \emptyset_i''''(x_1)\right)\left(1-\sum_{i=1}^{n} C_i\emptyset_i(x_1)+\sum_{i=1}^{n} D_i\emptyset_i(x_2)\ \right)^2 dx_1$$
$$= \alpha(V_{DC})^2\int_0^1 \emptyset_j(x_1)\left(\ 1\ +\frac{\delta\ 0.65\ d}{b}\left(1-\sum_{i=1}^{n} C_i(t)\emptyset_i(x_1) + \sum_{i=1}^{n} D_i(t)\emptyset_i(x_2)\right)\right)dx_1 \qquad (26)$$

$$\int_0^1 \emptyset_j(x_2)\left(\sum_{i=1}^{n} D_i \emptyset_i''''(x_2)\right)\left(1-\sum_{i=1}^{n} C_i \emptyset_i(x_1)+\sum_{i=1}^{n} D_i \emptyset_i(x_2)\right)^2 dx_2$$
$$= -\eta\alpha(V_{DC})^2 \int_0^1 \emptyset_j(x_2)\left(1+\frac{\delta\, 0.65\, d}{b}\left(1 - \sum_{i=1}^{n} C_i(t)\emptyset_i(x_1)+\sum_{i=1}^{n} D_i(t)\emptyset_i(x_2)\right)\right) U(x_2-\xi)\, dx_2 \quad (27)$$

3.2. Convergence Analysis and Validation

In this section, we neglect the Fringing-field effect and consider the parallel palate electrostatic force model by setting the parameter $\delta = 0$. We solve numerically the governing equations of the static problem given by Equations (26)-(27) while varying the value of the DC voltage. We first analyze the convergence behavior of the static response as the number of mode shapes is increased from 1 to 4. The results are shown in Figure 3.1. Similar to the typical static response of electrostatic actuators, the curves show an increasing trend in the beam deflection as the DC voltage increases until reaching the pull-in instability. We note that only the stable branch of solutions is shown in Figure 3.1. The use of 3 modes is observed to lead to an acceptable convergence of the static response of the coupled system. For the subsequent analysis, the same number of modes is considered.

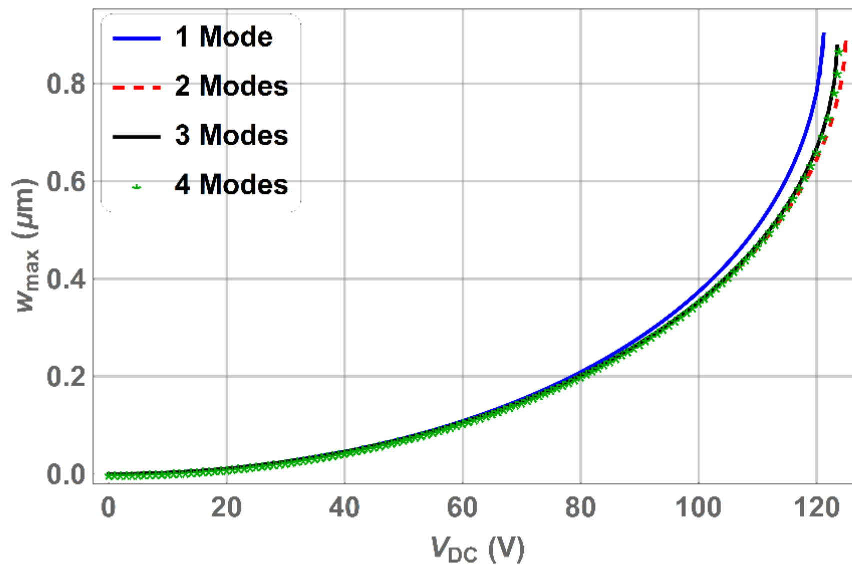

Figure 3.1: Static Pull-in convergence

To verify the numerical prediction of the developed reduced-order model given by Equations (26)-(27), we simulate the static response of the microbeam system under DC excitation using the finite element software ANSYS. A convergence analysis is carried out to obtain invariant simulation results under mesh refinement. As shown in Figure 3.2, the results obtained from the present model compare very well with the numerical simulations based on the finite element model.

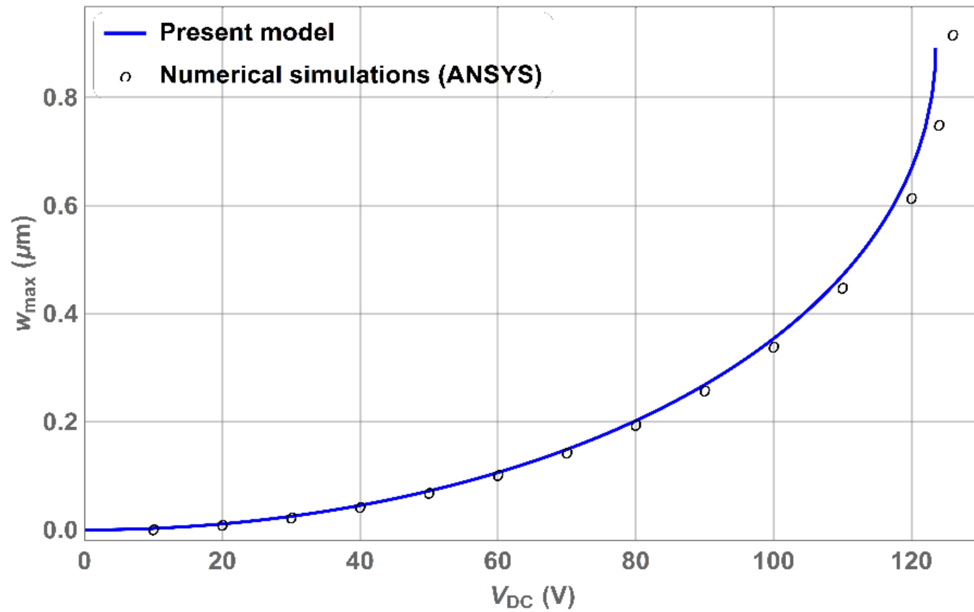

(a) Static response

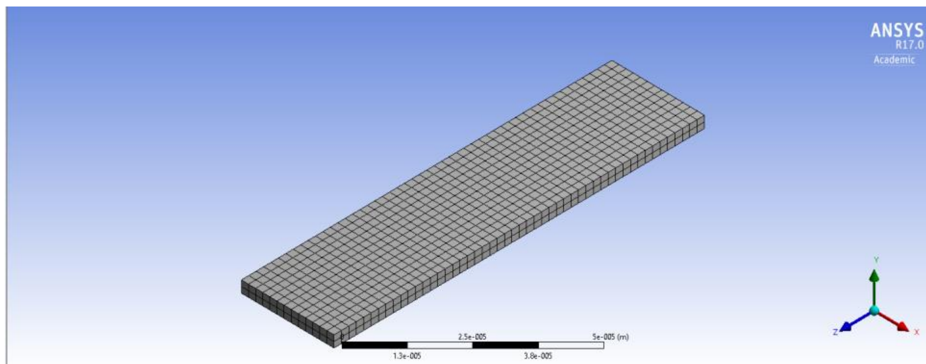

(b) FE model (ANSYS)

Figure 3.2: Static response to DC excitation for case study 1: comparison against numerical results obtained from finite element (FE) model in ANSYS

3.3. Static Response based on Parallel-plate Model

We use the reduced-order model to obtain the static response of the microsystem under DC actuation for all case studies reported in Table 3.2. The simulation results are displayed in Figure 3.3. We note that the response corresponding to the coupled dual beam system is taken as the maximum relative distance between the two vibrating beams until the occurrence of pull-in (i.e., they touch each other). We observe that the dual beam resonator is more sensitive to DC actuation and the pull-in voltage is lower when compared to the single beam case (with fixed electrode). The relative distance between the two movable beams for the dual beam resonator is found the same as the displacement of the single beam system just before the occurrence of the pull-in. This distance is about 0.88 μm. The present results are in good agreement with those obtained numerically by Ilyas et al. [34]. The vertical dashed lines in Figure 3.3(a) denote the experimental values of the pull-in voltage obtained by Ilyas et al. [34] by varying the voltage against current using Keithley parameter analyzer. The numerical predictions of the static pull-in voltages are close to their experimental counterparts.

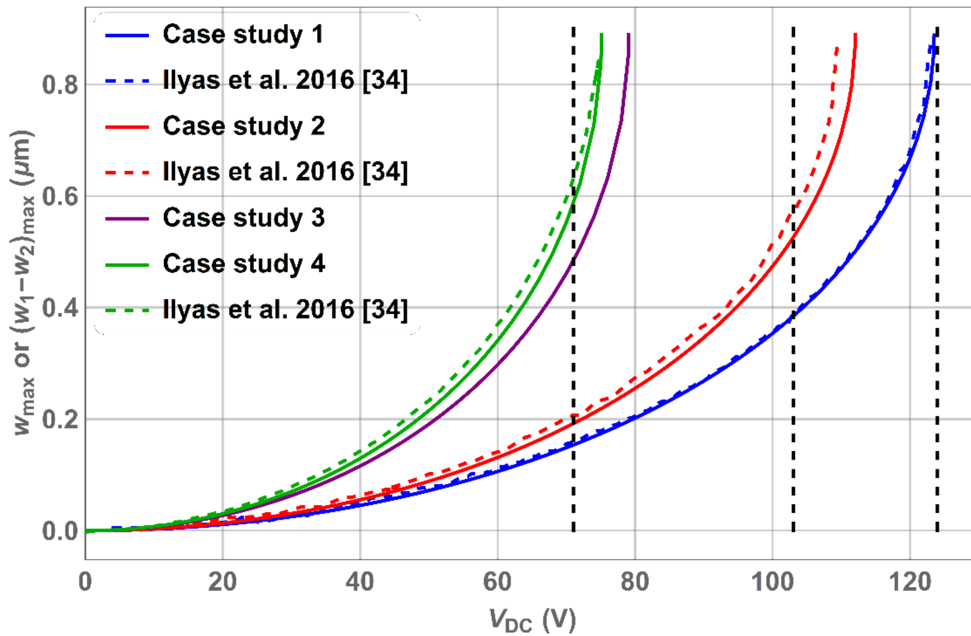

(a) Case studies 1-4.

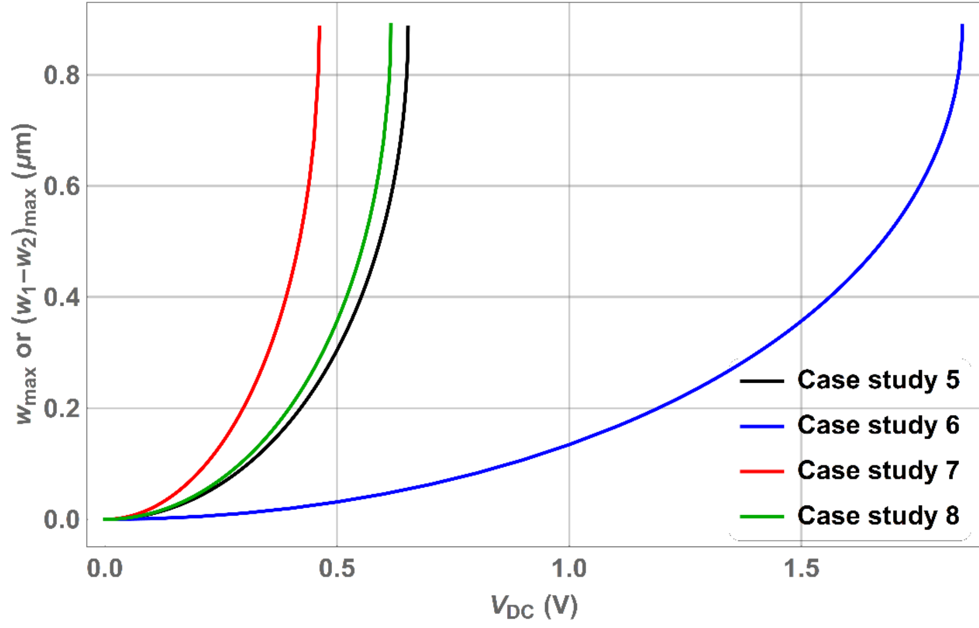

(b) Case studies 5-8.

Figure 3.3: Static response to DC excitation for the different case studies (dual and single beam systems): comparison against previous works. The vertical dashed lines denote the experimental values of the pull-in voltage obtained by Ilyas et al. [34].

The maximum distance between the single beam and the fixed electrode is denoted by w_{max} . For the dual beam case, the maximum relative distance between the two microbeams for is denoted by $(w_1 - w_2)_{max}$.

The static pull-in voltage of the single beam (uncoupled actuation) can be approximated by the following analytical expression [1]

$$V_{pull-in} = \sqrt{\frac{1.72}{\alpha_1}} \tag{28}$$

As for the dual beam case (coupled actuation) when considering identical beams (i.e., β= 1), the static pull-in voltage can be approximated as [34]

$$V_{pull-in} = \sqrt{\frac{0.868}{\alpha_1}} \tag{29}$$

Table 3.1 presents the values of the pull-in voltage obtained for all cases under investigation. The pull-in voltages obtained from the present study are compared to those reported in previous theoretical and experimental studies when considering similar beam configurations. A good agreement between the two sets of data is obtained. This demonstrates the capability of the current numerical model to predict accurately the static pull-in voltage. We note that the analytical formulas given by Equations (28) and (29) provide good approximation of the pull-in voltages for both single and dual beam cases. However, this is only valid when considering identical beams for the dual beam resonator and here comes the need for the numerical model to simulate any generic case. As expected, longer and/or thinner beam, being less stiff and having the tendency to bend more, leads to lower pull-in voltages. A reduction of 29-36% in the pull-in voltage is obtained when switching from the single beam case (uncoupled actuation) to dual beam case (coupled actuation). As such, dual beam microsystems seem to be more attractive for switching applications due to low power requirements to trigger the pull-in. Moreover, the relative travel distance between the two movable beams for the dual beam resonator is found to be the same as the distance traveled by the single beam system just before the occurrence of the pull-in.

Table 3.1: Static Pull-in voltages obtained for the cases under consideration (coupled and uncoupled actuation): comparison against previous theoretical and experimental studies.

Case study	Theoretical Present (V)	Analytical approximation equations (28)-(29) (V)	Theoretical Previous studies [34], [23] (V)	Experimental Previous studies [34] (V)
1	123.5	125	123.4	124
2	112	113.5	109.5	103
3	79	80.5	78.9	-
4	75.1	-	74.9	71
5	0.6529	0.6616	0.652	-
6	1.847	1.871	-	-
7	0.4617	0.47	-	-
8	0.61557	-	-	-

We examine the effect of the DC voltage on the pull-in time (i.e., the switching time taken by the microbeam to touch the other fixed/movable electrode at the occurrence of the pull-in). We consider case studies 5 and 7 that correspond to single

and dual beam configurations, respectively, to investigate the influence of the microsystem's design on the switching time. The obtained results are shown in Figure 3.4. Increasing the DC voltage beyond the pull-in voltage speeds up the snap-through of the beams. Clearly, the dual beam design enables a significant improvement in the switching time when compared to the single beam case. The dual beam system reduces the switching time by 35% to 45% for a DC voltage up to 1 V. These observations are consistent with the results reported by Ilyas et al. [34] and show the potential use of dual beam resonators as MEMS switches which are expected to trigger quickly a signal in response to a mechanical shock to activate safety functionalities such as airbag systems. This will be investigated in the next section when analyzing the dynamic response of the microsystem under mechanical shock.

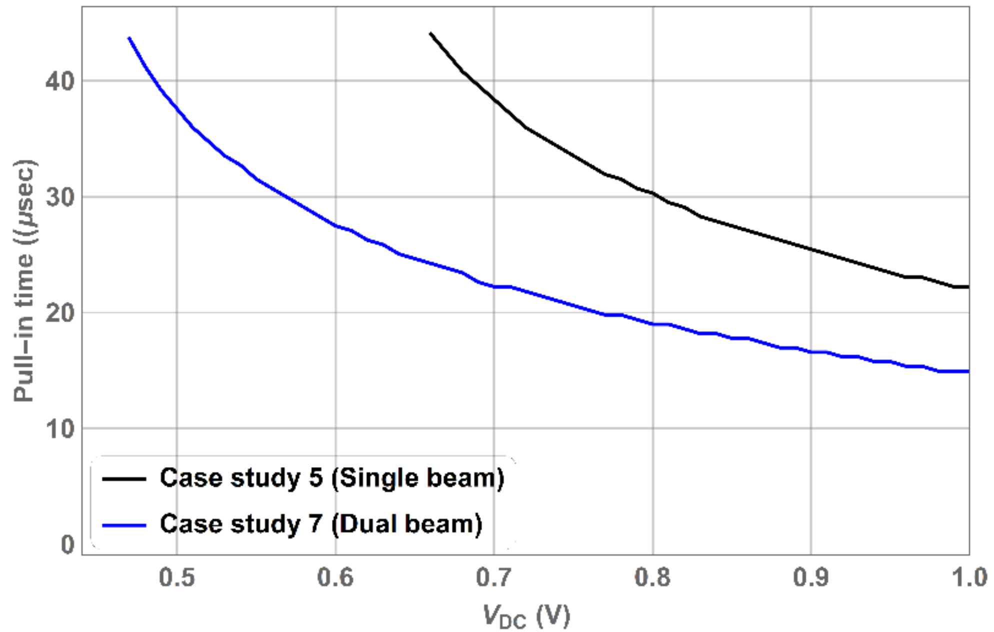

Figure 3.4: Variations of the switching time with the DC voltage for the single and dual beam cases.

3.4. Static Response: Fringing Field Effect

Setting the parameter δ equal to 1 Equations (24) and (25) allows for considering the Fringing-fields effect via the Palmer model. By simulating the equations, we observe a significant difference in pull-in voltages between the two electrostatic models; Parallel-plates and Palmer models. A % 4.24 reduction in the pull-in voltage is observed for both single and dual beams when accounting for the fringing-

fields. Moreover, the overall deflection of the microbeam is also affected as shown in Figure 3.5.

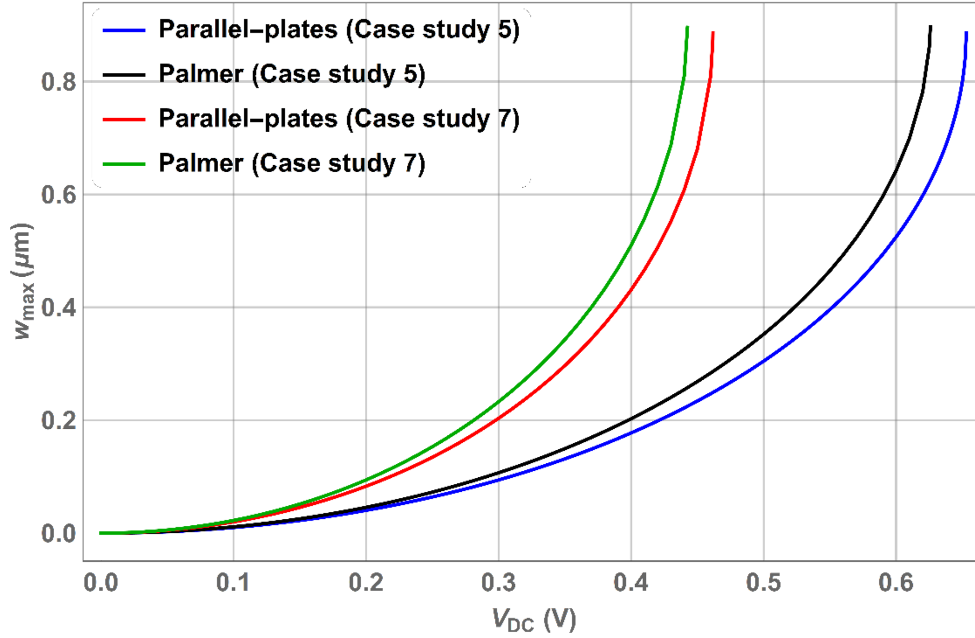

Figure 3.5: Static response to DC excitation for single and dual beams under Parallel plate and Palmer electrostatic models

To gain a better understanding of the microsystem behavior, we conduct a parametric study to test the response of different microbeam dimensions to Fringing field effect. First, we vary the width denoted by b of the single and dual beams and record the static pull-in voltage as shown in Table 3.2. We notice that, for all values of different microbeam widths, the Parallel-plate model gives the exact same pull-in voltage. On the other hand, Palmer model shows a significant change in pull-in voltage when varying the microbeam width. In particular, this change becomes steep for thinner microbeams, that is smaller width microbeams ($b<<1$) as shown in Figure 3.6.

Table 3.2: Pull-in voltage difference between Parallel-plate and Palmer models of electrostatic force while varying the microbeam width (b)

b (μm)	Single beam pull-in voltage (V)			Dual beam pull-in voltage (V)		
	Parallel-plate	Palmer	%Diff	Parallel-plate	Palmer	%Diff
10	**0.6529**	**0.6258**	**%4.24**	**0.46167**	**0.4425**	**%4.24**
9	0.6529	0.6231	%4.67	0.46167	0.4406	%4.67
8	0.6529	0.6196	%5.23	0.46167	0.4381	%5.23
7	0.6529	0.6153	%5.92	0.46167	0.4351	%5.92
6	0.6529	0.6097	%6.84	0.46167	0.4311	%6.84
5	0.6529	0.6022	%8.08	0.46167	0.4258	%8.08
4	0.6529	0.5914	%9.89	0.46167	0.4182	%9.89
3	0.6529	0.5747	%12.7	0.46167	0.4064	%12.7
2	0.6529	0.5454	%17.9	0.46167	0.3857	%17.9
1	0.6529	0.4797	%30.6	0.46167	0.3392	%30.6

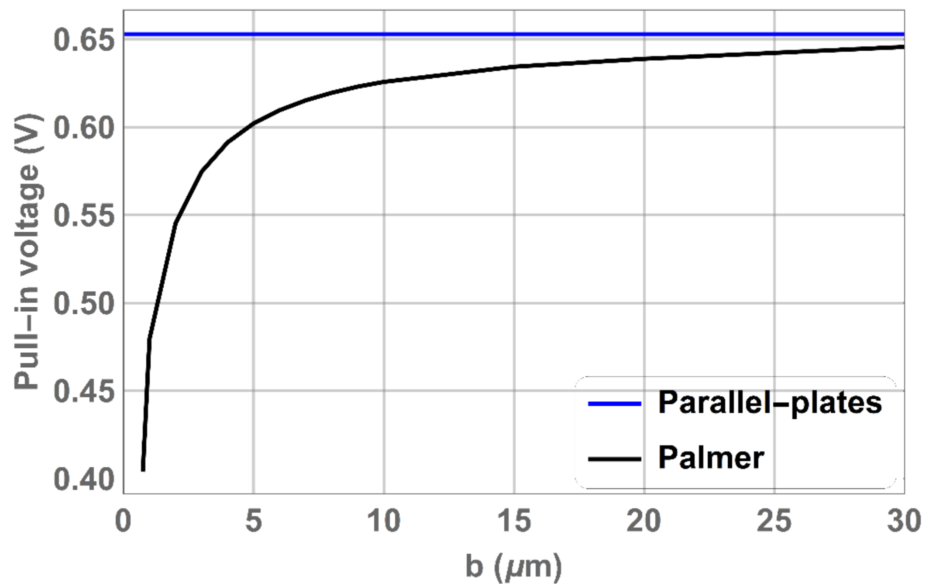

Figure 3.6: Pull-in voltage for different beam widths (Case study 5)

Next, we examine the impact of the gap distance (the initial distance between the microbeam and the fixed electrode) on the static response for the single beam and

(initial distance between the two microbeams) for the dual beam case. The gap distance denoted by d is varied and the pull-in voltage for each case is computed and reported in Table 3.3. It can be noted that, for the single beam and dual beam cases, the two electrostatic models namely parallel plates and Palmer, deviate when increasing the gap distance as shown in Figure 3.7. Furthermore, no significant difference of the Fringing-fields effect on the dual beam in comparison with the single beam is observed at high and moderate gap distances. However, at smaller gap distances, the Fringing-fields effect has more pronounced impact on the dual beam case in comparison with single beam case.

Table 3.3: Pull-in voltage difference between Parallel-plate and Palmer models of electrostatic force when varying the gap distance (d)

d (μm)	Single beam pull-in voltage (V)			Dual beam pull-in voltage (V)		
	Parallel-plate	Palmer	%Diff	Parallel-plate	Palmer	%Diff
12	9.595	7.789	%20.8	6.7852	5.5082	%20.8
9	6.232	5.286	%16.4	4.4071	3.7377	%16.4
7	4.275	3.742	%13.3	3.023	2.6464	%13.3
5	2.58	2.337	%9.88	1.8249	1.653	%9.89
3	1.199	1.127	%6.19	0.8481	0.7971	%6.2
2.5	0.9124	0.866	%5.22	0.6452	0.6123	%5.23
2	**0.6529**	**0.6258**	**%4.24**	**0.4616**	**0.4425**	**%4.23**
1.5	0.424	0.4106	%3.21	0.2998	0.2904	%3.19
1	0.23	0.2258	%1.84	0.1632	0.1597	%2.17

We conclude that, for MEMS system designs having a ratio of $\left(\frac{b}{d}\right) \ll 1$, the Fringing field represented by Palmer model has a dominant effect and its corresponding static response greatly deviates from that obtained from the Parallel plate model. For example, for the case $\left(\frac{b}{d}\right) = 0.0833$, a 58.8% is the percentage difference between pull-in voltages obtained from the two models for the single beam case. $V_{pull-in} = 9.595$ V is obtained from parallel plates model, and $V_{pull-in} = 3.953$V is found when accounting for the Fringing field via Palmer model.

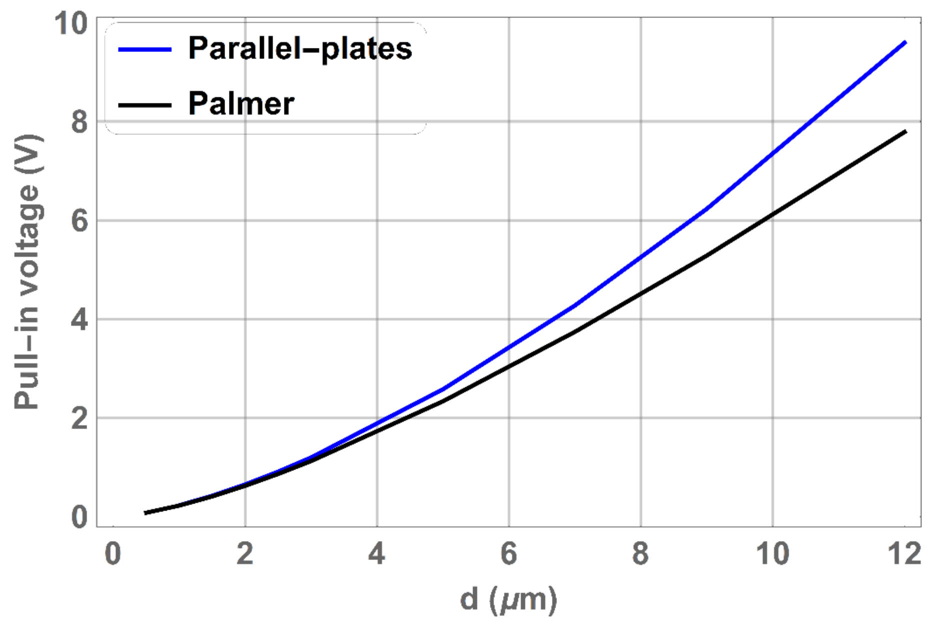

Figure 3.7: Pull-in voltage for different gap distances (Case study 5)

Chapter 4. Dynamic Analysis of Electrically-actuated Microbeams

In this chapter, we formulate and solve the eigenvalue problem to compute the natural frequencies of the electrically-actuated microbeams under DC voltage when accounting for the Fringing-field effect. We also generate the frequency-response curves when activating the AC voltage.

4.1. Natural Frequencies under Electrostatic Forcing

Operating near resonance is recommended for several applications such as resonant sensors and filters to amplify the microbeam motion and achieve higher output signal or to trigger the pull-in instability (e.g., microswitches). As such, we follow Younis [1] to formulate the eigenvalue problem and evaluate the natural frequencies of the coupled system under electrostatic forcing. To do so, the deflections of the microbeams are split into a static component, resulting from the DC actuation, $w_{1,2}^{s}(x_{1,2})$ and a dynamic component $w_{1,2}^{d}(x_{1.2},t)$:

$$w_{1,2}(x_{1,2},t) = w_{1,2}^{s}(x_{1,2}) + w_{1,2}^{d}(x_{1,2},t) \tag{30}$$

Substituting Equation (30) into Equations (16) and (17), dropping the damping, mechanical shock, and SQFD terms, linearizing the nonlinear electrostatic forcing around the static position, and the first-order terms in $w_{1,2}^{d}$ results in the following linearized equation:

$$\begin{aligned}\ddot{w}_1^d(x_1,t) + \left(w_1^d(x_1,t)\right)'''' \\ = \frac{2\alpha(V_{DC})^2}{\left(1 - w_1^s(x_1) + w_2^s(x_2)\right)^3}\Bigg(1 + \frac{\delta\, 0.65\, d}{b}\big(1 - w_1^s(x_1) \\ + w_2^s(x_2)\big)\Bigg)\left(w_1^d(x_1,t) - w_2^d(x_2,t)\right)\end{aligned} \tag{31}$$

$$\beta \ddot{w}_2^d(x_2,t) + \left(w_2^d(x_2,t)\right)'''' = \frac{-2\alpha\eta(V_{DC})^2}{\left(1 - w_1^s(x_1) + w_2^s(x_2)\right)^3}\left(1 + \frac{\delta\, 0.65\, d}{b}\left(1 - w_1^s(x_1) + w_2^s(x_2)\right)\right)\left(w_1^d(x_1,t) - w_2^d(x_2,t)\right) \quad (32)$$

To solve the eigenvalue problem associated with the above linearized equations and obtain the natural frequencies of the coupled system, we use again the Galerkin method and expand the dynamic components as

$$w_1^d(x_1,t) = \sum_{i=1}^{n} u_i(t)\emptyset_i(x_1) \quad (33)$$

$$w_2^d(x_2,t) = \sum_{i=1}^{n} v_i(t)\emptyset_i(x_2) \quad (34)$$

Substituting Equations (33) and (34) into Equations (31) and (32), multiplying the outcome by $\emptyset_j$and integrating the resulting equations from 0 to 1, we obtain

$$\sum_{i=1}^{n} \ddot{u}_i(t)\int_0^1 \emptyset_j(x_1)\emptyset_i(x_1)\,dx_1 + \sum_{i=1}^{n} u_i(t)\int_0^1 \emptyset_j(x_1)\emptyset_i''''(x_1)dx_1 = \sum_{i=1}^{n}\left[\int_0^1 \emptyset_j(x_1)\,\emptyset_i(x_1)\frac{2\alpha(V_{DC})^2}{\left(1 - w_1^s(x_1) + w_2^s(x_2)\right)^3}\left(1 + \frac{\delta\, 0.65\, d}{b}\left(1 - w_1^s(x_1) + w_2^s(x_2)\right)\right)dx_1\right]\left(u_i(t) - v_i(t)\right) \quad (35)$$

$$\beta\sum_{i=1}^{n} \ddot{v}_i(t)\int_0^1 \emptyset_j(x_2)\emptyset_i(x_2)\,dx_2 + \sum_{i=1}^{n} v_i(t)\int_0^1 \emptyset_j(x_2)\emptyset_i''''(x_2)dx_2 = \sum_{i=1}^{n}\left[\int_0^1 \emptyset_j(x_1)\emptyset_i(x_1)\frac{2\alpha(V_{DC})^2}{\left(1 - w_1^s(x_1) + w_2^s(x_2)\right)^3}\left(1 + \frac{\delta\, 0.65\, d}{b}\left(1 - w_1^s(x_1) + w_2^s(x_2)\right)\right)dx_2\right]\left(u_i(t) - v_i(t)\right) \quad (36)$$

Replacing the term $\emptyset_i''''$ by $\omega_i^2 \emptyset_i$ and making use of the mode shapes orthogonality, we simplify the Equations (35) and (36)

$$\ddot{u}_j(t) + \omega_i^2 u_j(t) = \alpha (V_{DC})^2 \sum_{i=1}^{n} \left[\int_0^1 \emptyset_j(x_1)\, \emptyset_i(x_1) \left(\frac{2}{\left(1 - w_1^s(x_1) + w_2^s(x_2)\right)^3} + \frac{\delta\, 0.65\, d}{b\, \left(1 - w_1^s(x_1) + w_2^s(x_2)\right)^2} \right) dx_1 \right] \left(u_j(t) - v_j(t) \right) \tag{37}$$

$$\beta \ddot{v}_j(t) + \omega_i^2 v_j(t) = -\eta \alpha (V_{DC})^2 \sum_{i=1}^{n} \left[\int_0^1 \emptyset_j(x_2)\, \emptyset_i(x_2) \left(\frac{2}{\left(1 - w_1^s(x_1) + w_2^s(x_2)\right)^3} + \frac{\delta\, 0.65\, d}{b\, \left(1 - w_1^s(x_1) + w_2^s(x_2)\right)^2} \right) dx_2 \right] \left(u_j(t) - v_j(t) \right) \tag{38}$$

Equations (37) and (38) can be expressed in matrix form as

$$\begin{bmatrix} \ddot{u}_1 \\ \ddot{u}_2 \\ \vdots \\ \ddot{u}_n \\ \ddot{v}_1 \\ \ddot{v}_2 \\ \vdots \\ \ddot{v}_n \end{bmatrix} = M \begin{bmatrix} u_1 \\ u_2 \\ \vdots \\ u_n \\ v_1 \\ v_2 \\ \vdots \\ v_n \end{bmatrix} \tag{39}$$

where M is 2n x 2n matrix and its constant coefficients are:

For i =1 … n and j =1 … n

$$M_{i,j} = \delta_{i,j} \omega_i^2 - \alpha (V_{DC})^2 \int_0^1 \emptyset_j(x_1) \left(\frac{2}{\left(1 - w_1^s(x_1) + w_2^s(x_2)\right)^3} + \frac{\delta\, 0.65\, d}{b\, \left(1 - w_1^s(x_1) + w_2^s(x_2)\right)^2} \right) dx_1 \tag{40}$$

For i =1…. n and j = n+1 … 2n

$$M_{i,j} = \alpha(V_{DC})^2 \int_0^1 \emptyset_j(x_1) \left(\frac{2}{\left(1 - w_1^s(x_1) + w_2^s(x_2)\right)^3} + \frac{\delta\, 0.65\, d}{b\left(1 - w_1^s(x_1) + w_2^s(x_2)\right)^2} \right) dx_1 \tag{41}$$

For $i = n$ +1…..2n and j =1 … n

$$M_{i,j} = \alpha(V_{DC})^2 \int_0^1 \emptyset_j(x_2) \left(\frac{2}{\left(1 - w_1^s(x_1) + w_2^s(x_2)\right)^3} + \frac{\delta\, 0.65\, d}{b\left(1 - w_1^s(x_1) + w_2^s(x_2)\right)^2} \right) dx_2 \tag{42}$$

For $i = n$+1…. 2n and j =1…. n

$$M_{i,j} = \delta_{i,j} \frac{1}{\beta} \omega_i^2 - \alpha(V_{DC})^2 \int_0^1 \emptyset_j(x_2) \left(\frac{2}{\left(1 - w_1^s(x_1) + w_2^s(x_2)\right)^3} + \frac{\delta\, 0.65\, d}{b\left(1 - w_1^s(x_1) + w_2^s(x_2)\right)^2} \right) dx_2 \tag{43}$$

where $\delta_{i,j} = 1$ if i = j otherwise 0. To compute the natural frequencies of the coupled system under DC excitation, we first determine the static deflections of the microbeams $w_1^s(x_1, t)$ and $w_2^s(x_2, t)$ by solving Equations (26) and (27), compute the coefficients $M_{i,j}$ as given by Equations (40)-(43), and then calculate the eigenvalues of the matrix M. The natural frequencies are obtained by taking the square roots of these eigenvalues.

Figure 4.1 displays the variations of the natural frequencies with the DC voltage for the different cases under investigation. Some results as shown in Figure 4.1 (a) are compared to those obtained numerically by Ilyas et al. [34]. Again, a good agreement between the two sets of data is observed. Shorter and/or thicker beams result in higher natural frequencies as can be seen in Figure 4.1 (a) and Figure 4.1 (b) while lower values are obtained when considering electrically-coupled beams in comparison to the single beam actuated by a fixed electrode. This indicates the possible use of dual beam resonators when lower operating frequency range is required.

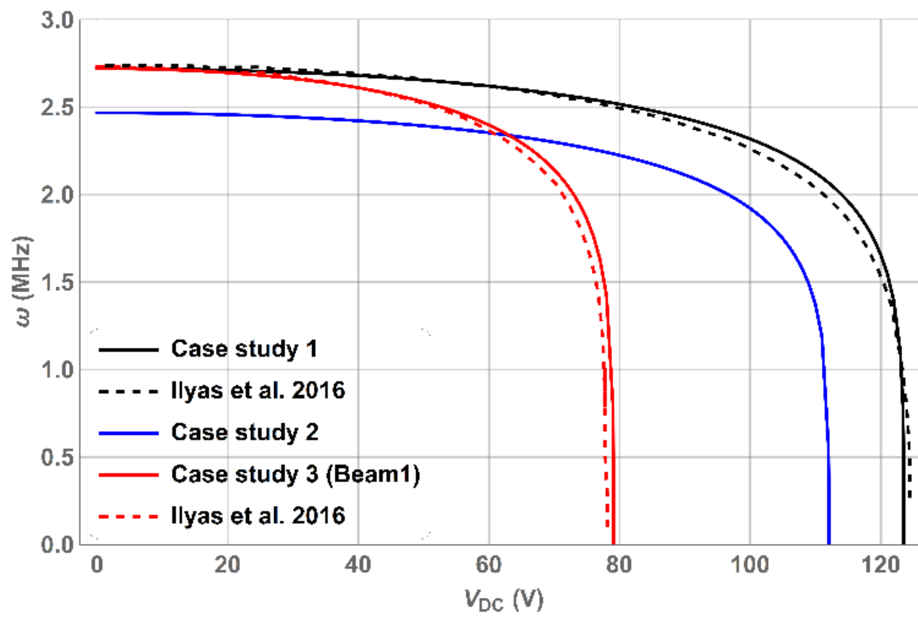

(a) Case studies 1-3

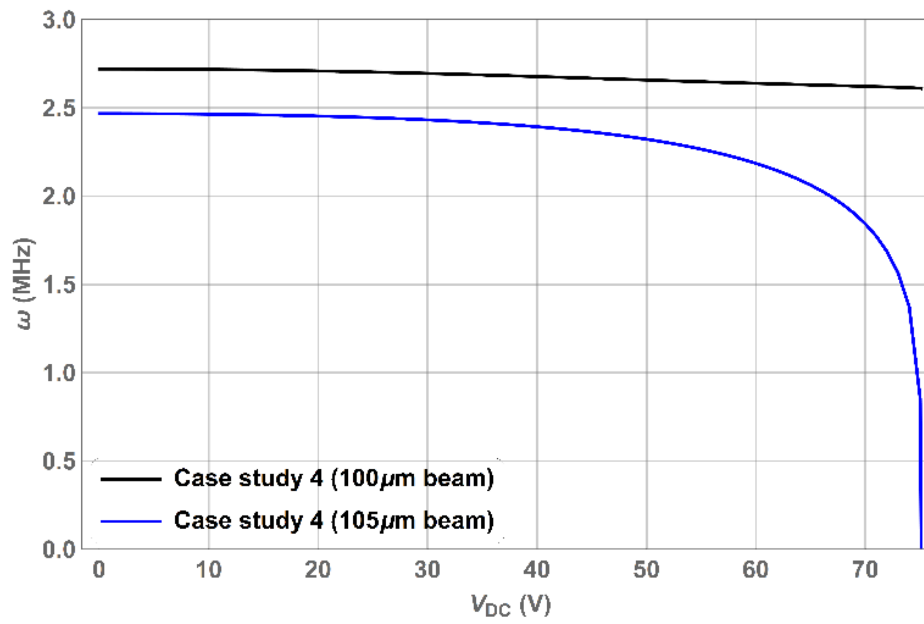

(b) Case study 4

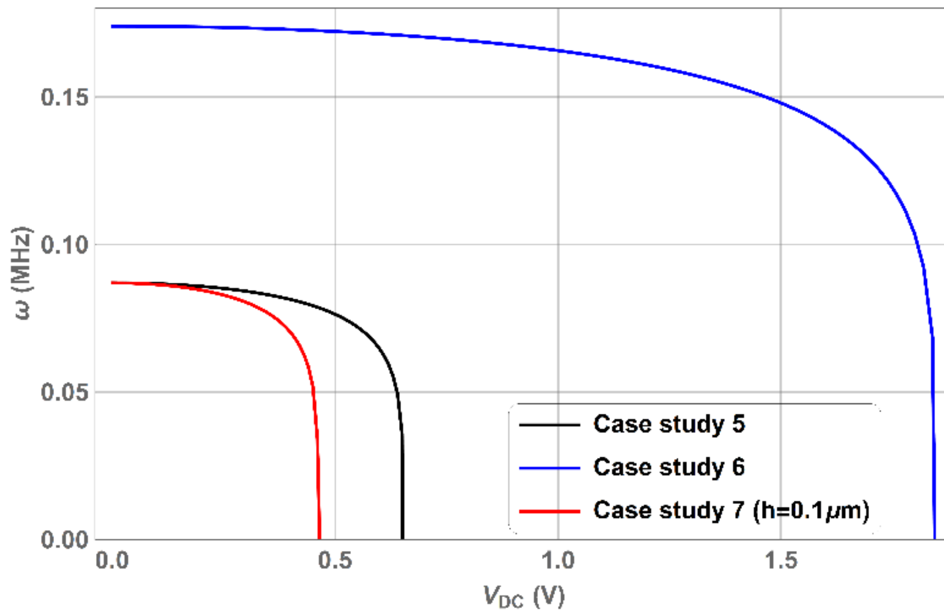

(c) Case studies 5-7

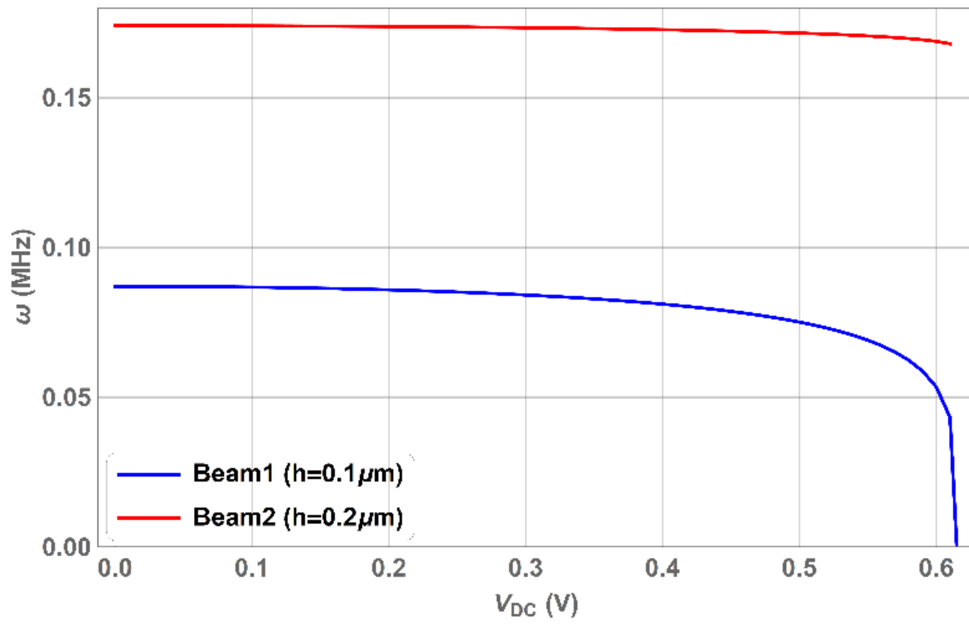

(d) Case study 8

Figure 4.1: Variations of the natural frequency with the DC voltage for the different case studies (dual and single beam systems): comparison against previous works. Note that the results obtained by Ilyas et al. [34] are originally reported in the nondimensional form

Next, we study the effect of the fringing-fields on the system's natural frequency by considering the Palmer model. As shown in Figure 4.2, incorporating the Fringing field results in lower frequencies given the voltage. The graph shows also a lower pull-in voltage when accounting for the Fringing field effect as demonstrated by the sharp drop in the natural frequency. Again, the difference in the natural frequency obtained when using the two electrostatic forcing terms (with and without Fringing field impact) is larger when considering a smaller width-to-gap ratio.

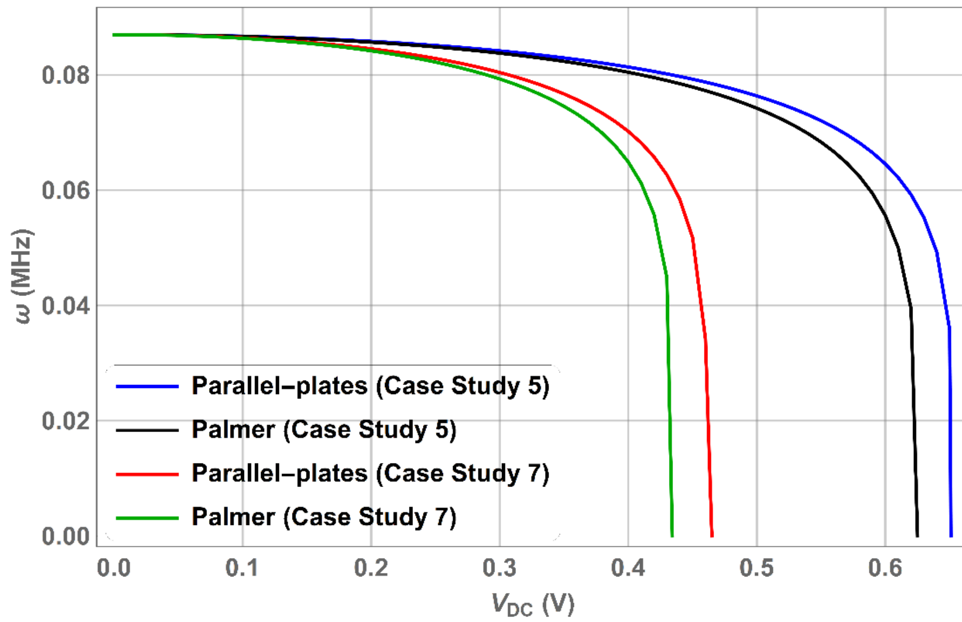

Figure 4.2: Effect of fringing fields on the natural frequency of single and dual beams

4.2. Frequency Response: Effect of Electric Actuation and Microsystem Design

We activate the AC excitation and examine the dynamic response of the microsystems for the cases under study. Figure 4.3 displays the frequency responses of the microsystems for different AC and DC voltages near the primary resonance as identified in the previous section. Figure 4.3 (a) and (b) show that the increase in the DC voltage shifts the frequency response curves to the left due to the softening effect of the electrostatic forcing. Clearly, varying the AC voltage affects significantly the frequency-response curves. As expected, increasing the AC voltage results in the amplification of the microbeam motion. For low AC and DC voltages, the system behavior is nearly-linear. For higher AC excitation, we observe the occurrence of dynamic pull-in bandwidth in the frequency response curves; that is, only unstable

solutions of the microbeam dynamics. For instance, the analysis of case study 1 (single beam) shows that the fold bifurcation (turning point) takes place at 2.38 MHz when setting the DC and AC voltages equal to 95 V and 7 V, respectively (see Figure 4.3(a)). Operating with an excitation frequency between 2.38 MHz and 2.5 MHz results in the dynamic pull-in. The frequency response curves exhibit expanded pull-in bandwidth when operating the dual-beam systems near the primary resonance. Figure 4.3 (b) shows that the pull-in bandwidth reaches 250 kHz when actuating the microbeams at a DC voltage of 60 V and an AC voltage of 5 V. As shown in Figure 4.3 (c) and (d), the pull-in bandwidth increases from 5 kHz to 17 kHz when shifting from the single beam to the dual beam system (case studies 5 and 7) while applying a DC voltage of 0.2 V and an AC voltage of 0.15 V for both cases. This presents an undesirable effect for the reliability of some MEMS devices such as resonant sensors.

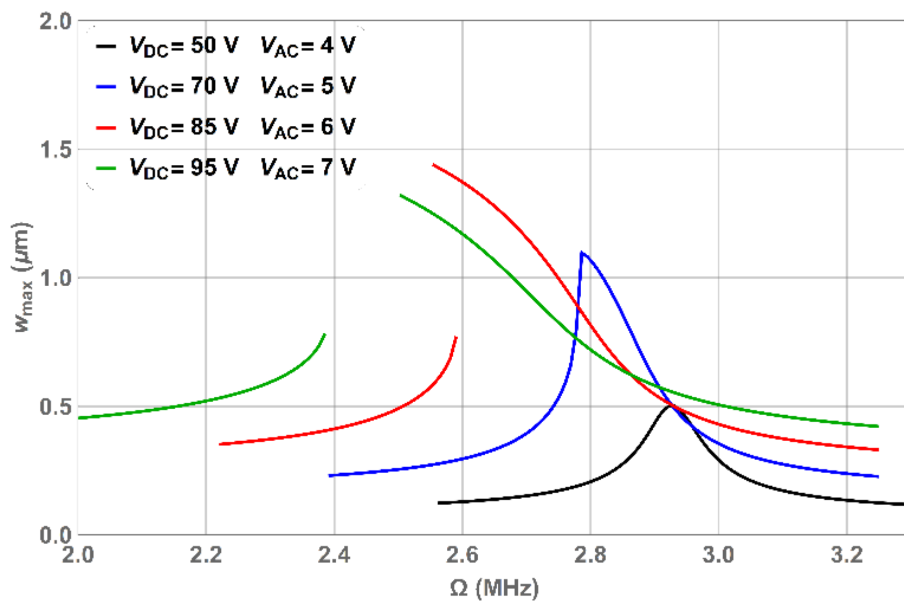

(a) Case study 1 (Single beam).

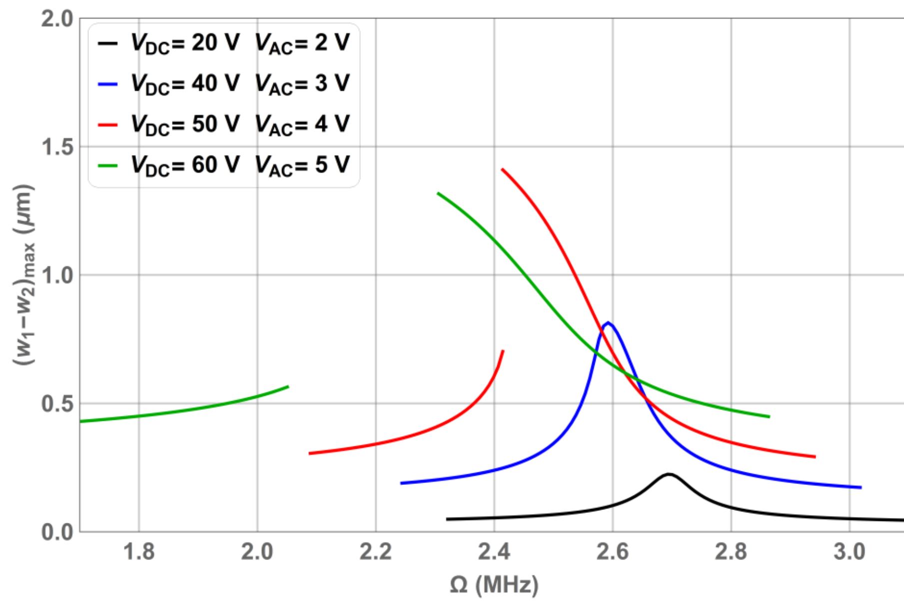

(b) Case study 3 (dual beam - identical).

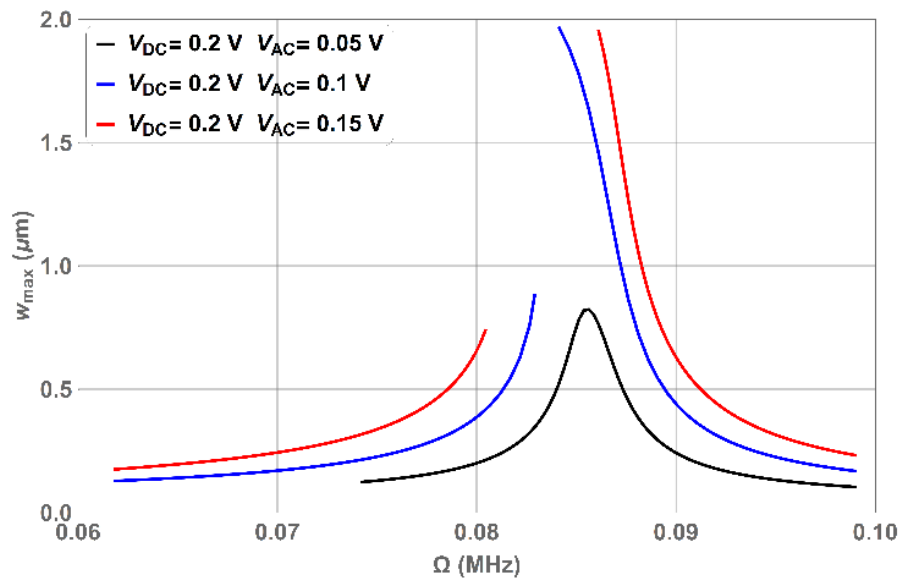

(c) Case study 5 (Single beam).

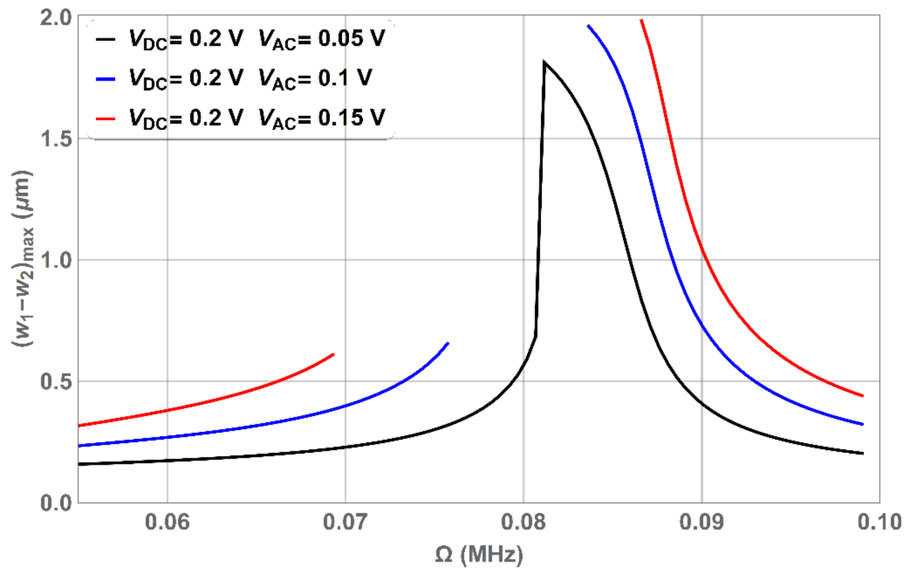

(d) Case study 7 (dual beam - identical).

Figure 4.3: Frequency response curves of the microsystem for varying DC and AC voltages for the different case studies (dual and single beam systems). Results are shown near the primary resonance

However, this phenomenon can be deployed to design MEMS switches that are triggered by the presence of gas [10, 12, 28], biological mass [7, 8, 9], or actuated at or beyond a specific level of mechanical shock or acceleration [21, 22, 23]. The frequency response curves of the dual beam system made of microbeams with different thickness shown in Figure 4.4 exhibit two peaks near the natural frequencies related to each microbeam at low AC and DC voltages. Inspecting these frequency response curves, we observe that higher amplitudes are obtained near the resonance frequency of the thinner microbeam being more flexible and then it is influenced more by the electrostatic coupling in comparison to the thicker microbeam. Higher electric actuation results in the appearance of two dynamic pull-in bandwidths in the frequency response curves. This indicates that dual beam systems composed of nonidentical beams seem to enable more tunability for switching applications but less control on the safe operation frequency range for other microsystems, which are expected to operate away from the pull-in instability.

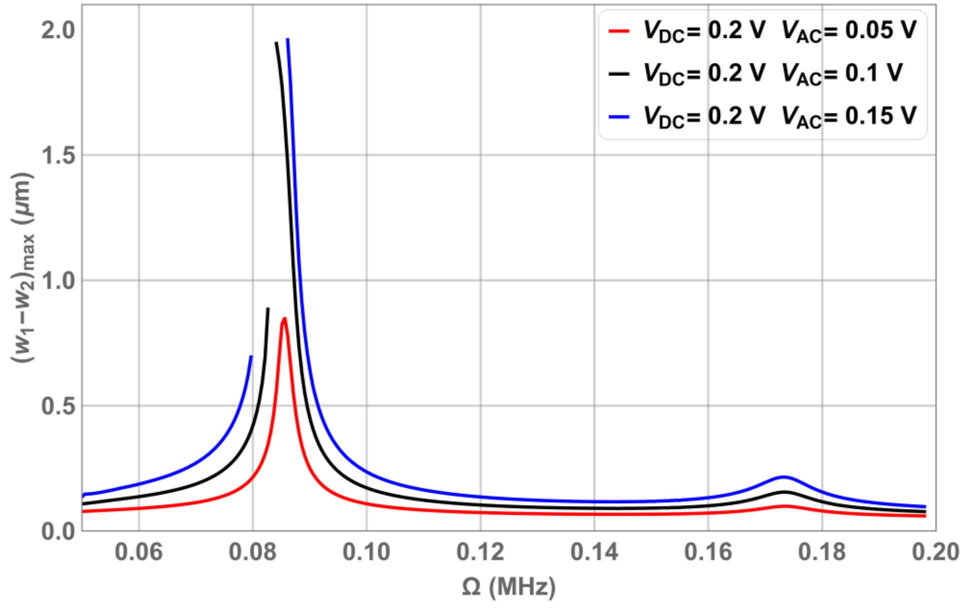

(a) $\mathrm{V_{DC}} = 0.2\ V$

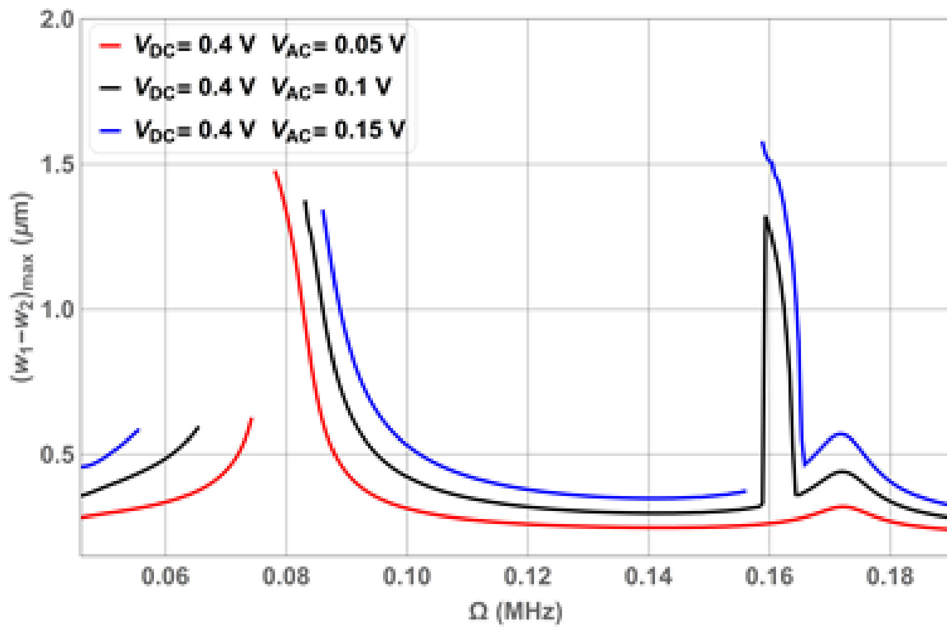

(b) $\mathrm{V_{DC}} = 0.4\ V$

Figure 4.4: Frequency response curves of the microsystem for varying DC and AC voltages for case study 8 (dual beam system). Results are shown near the primary resonance.

The subharmonic frequency of approximately 0.16 MHz causes interesting dynamics in the beams due to the square nonlinearity. It can be noted that the effect of this frequency is enabled at a certain AC voltage for a fixed DC voltage. In the present

case, an AC voltage of approximately 0.1 V enables the beams in case of 0.4 V to have an increase in their relative deflection. The subharmonic frequency effect on the microstructure appear interesting in some applications. For example, Younis [8] has proved that, for gas detection applications, operating near the subharmonic frequency of a single beam improves the sensitivity. Unlike the natural frequency, subharmonic frequency shows a sharp transition from low to high beam deflection due to a very small change in frequency.

Chapter 5. Shock Response of Electrically-actuated Microbeams

In this chapter, we consider the full mathematical model of the electrically-actuated microbeams under mechanical shock while accounting for the squeeze film damping and Fringing field effect. The effect of shock amplitude and duration under different DC and AC excitations is investigated for different case studies.

5.1. Effect of Microsystem Design on the Shock Response

Several research studies have reported failures in the operation of electrically actuated MEMS resonators when undergoing mechanical shocks. As such, we simulate the response of different designs of resonators (as outlined in Tables 3.1 and 3.2) under the combination of electrostatic forcing and mechanical shock. The objective of this study is twofold: to assess the robustness of the microstructure to withstand different levels of shock loads and to investigate the possible use of novel designs for switching applications. Figure 5.1 shows the shock function used in the dimensionless form.

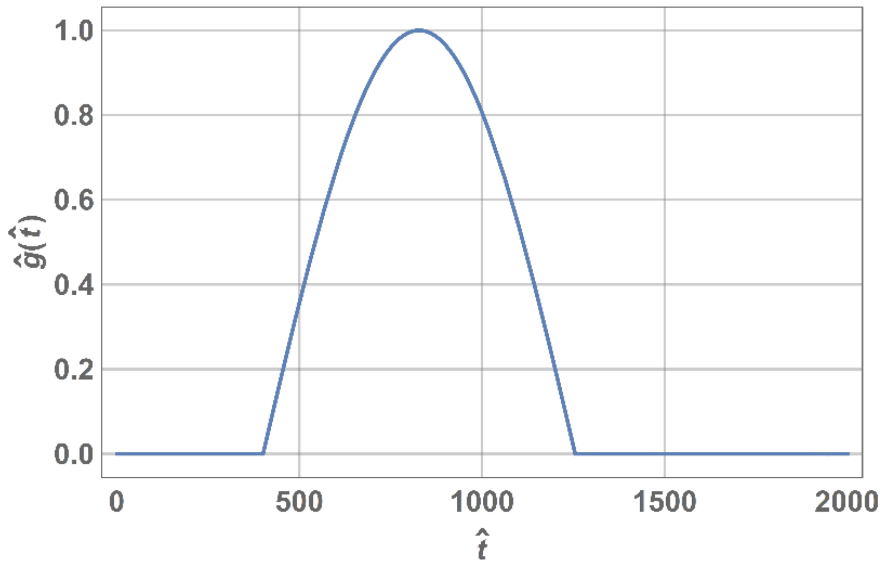

Figure 5.1: The considered shock function in the dimensionless form

Figure 5.2 show a linear decreasing trend in the dynamic pull-in voltage V_{DPI} for the single beam system (case study 1) when increasing the shock amplitude. The values of V_{DPI} are estimated by gradually increasing the applied DC voltage until the onset of the pull-in. The results are obtained for $V_{AC} = 0$ V and $V_{AC} = 6$ V and the shock duration T is set equal to 1 ms. High shock loading levels in the order of hundreds of thousands of g's. are required to reduce the pull-in voltage. The slopes are found equal

to $-1.137\ X10^{-4}$ and $-0.8625\ X10^{-4}$ for $V_{AC} = 0$ V and $V_{AC} = 6$ V, respectively. We show also the time histories obtained for different shock amplitudes while keeping the DC and AC voltages equal to 50 V and 6 V, respectively. Before reaching the critical value of the shock amplitude (${a_0}^c$= 419,000 g), we observe an amplification of the time response once the microsystem undergoes the mechanical shock and then followed by the recovery to the original oscillations. For shock amplitudes higher than ${a_0}^c$, the microbeam collapses and hits the fixed electrode.

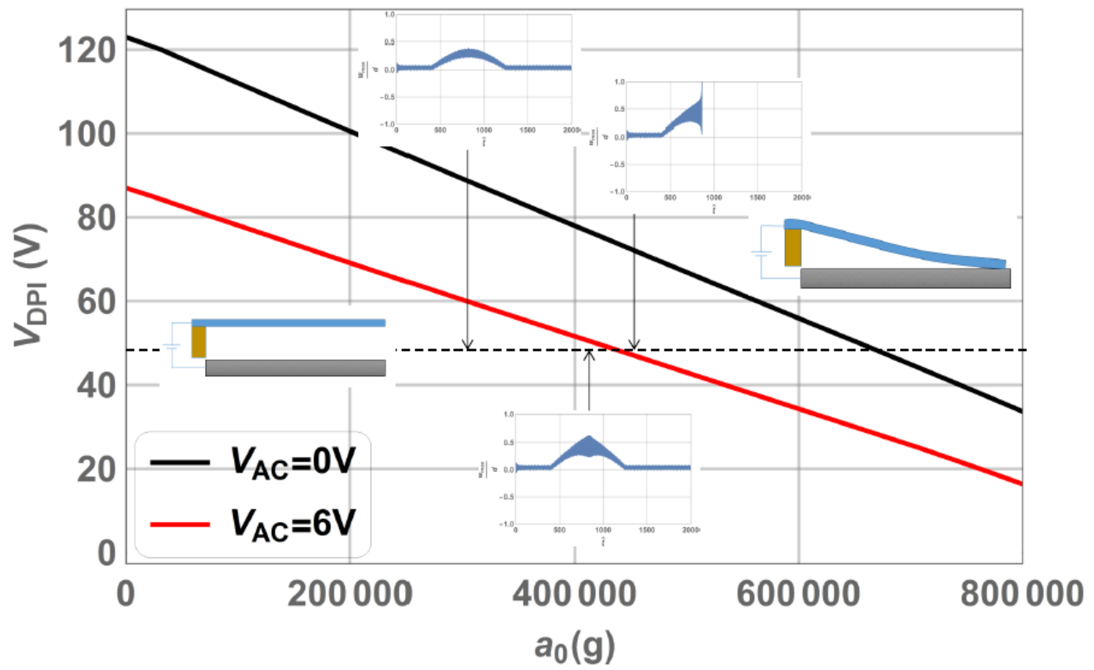

Figure 5.2: Variations of the dynamic pull-in voltage with the amplitude of the mechanical shock (case study 1)

To enhance the sensitivity of the microsystem to the mechanical shock, we consider thinner microbeams and analyze the dynamic response for case studies 5-8. We note case study 5 is similar to the one reported in [23]. The results are obtained when applying only DC voltage and mechanical shock with different pulse times (T = 1 ms and T = 0.1 ms). The present numerical predictions of the dynamic pull-in voltages compare well with those obtained by Younis et al. [23] using the finite element software ANSYS (see Figure 5.3). Of interest, we observe that the dual beam is much less sensitive to the mechanical shock when compared to the single-beam case. Similar observations can be made even when considering microbeams of different thickness (case study 8). The simulation results indicate that dual-beam systems are more robust

in terms of resistance to mechanical shock and provide a reliable design for the operation of MEMS devices in harsh environments characterized by high shock levels.

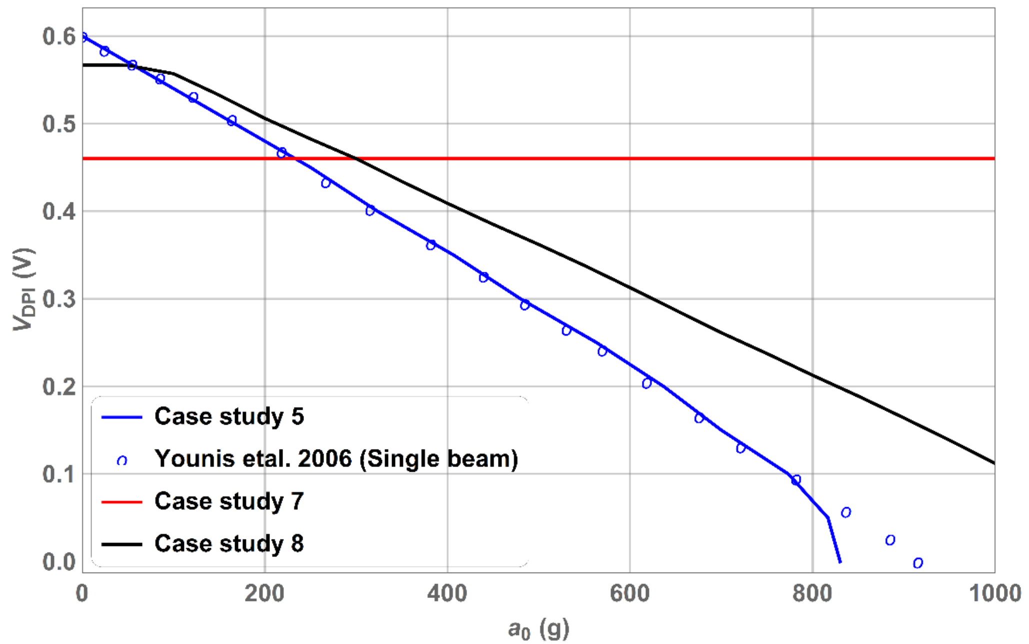

(a)

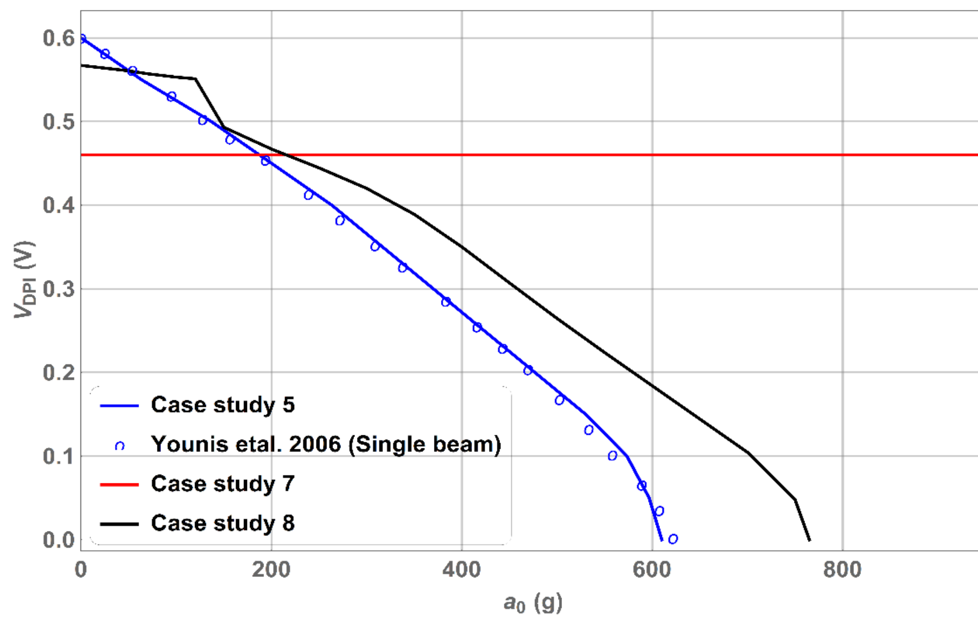

(b)

Figure 5.3: Variations of the dynamic pull-in voltage with the amplitude of the mechanical shock: (a) quasi-static ($T = 1$ ms) and (b) dynamic loading case ($T = 0.1$ ms). Results are compared to those reported by Younis et al. [23]

Figure 5.2 and Figure 5.3 show the possible tunability of switches (deploying single beams) with operation ranges varying from few hundreds to hundreds of

thousands of g's depending on the application of interest. For instance, microbeam systems sensitive to low g accelerations can be used for the detection of earthquake signals and the activation of other functionalities such as alarm or a network of sensors for seismic activity recording [22]. Switches operating at high shock levels are commonly used for military purposes [25] [26].

To examine the impact of the geometry on the system's response, we consider different dual beam thickness to simulate the asymmetric dual beam behavior under shock. We plot in Figure 5.4 the variations the dynamic pull-in voltage with the shock amplitude while varying the difference in the thickness of the two beams. Clearly, breaking the symmetry renders the dual beam system more sensitive to mechanical shock and results in the snap-through of the two beams at lower shock amplitudes. Setting $h_1$and h_2 equal to 0.1 μm and 0.2 μm, respectively, leads to similar trend as that of the single beam case. It can be noted that microbeam resistance to mechanical shock is gradually increasing as the two beam thicknesses approach to each other (as shown in Figure 5.4).

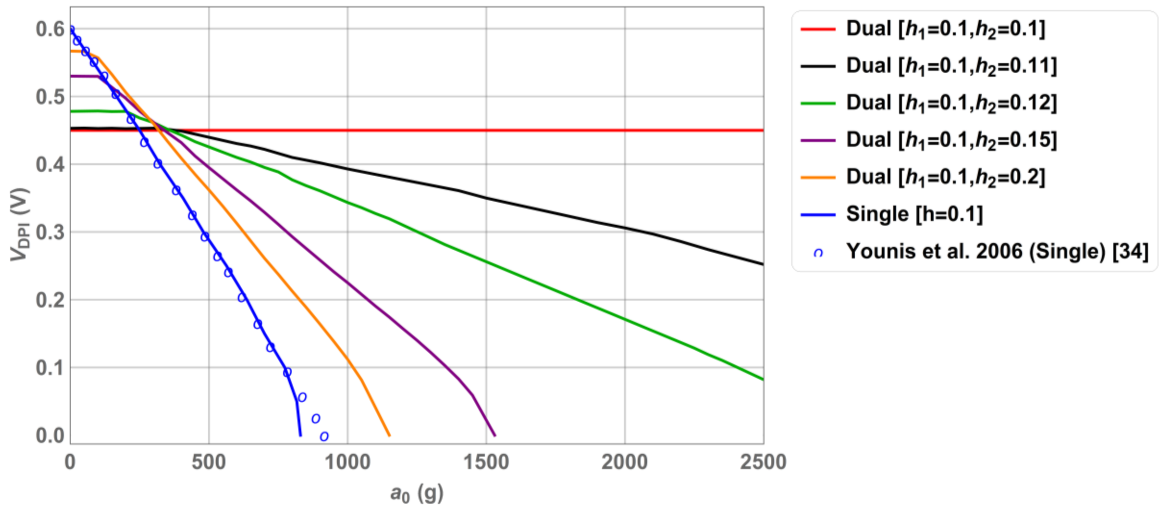

Figure 5.4: Variations of the dynamic pull-in voltage with the amplitude of the mechanical shock for different thickness under mechanical shock of 1 ms duration.

To examine the effect of the pulse time (shock duration) T on the dynamic response of the microbeam, we plot in Figure 5.5 the time histories of the tip deflection under combined impact of DC actuation and shock load for T =1 ms and T =0.1 ms (case study 5). The figure shows the stable and unstable responses. The dynamic pull-in for this single microbeam without accounting for the effect of the mechanical shock

is found equal to 0.6 V which is equal to the value reported by Younis et al. [18]. The time histories depicted in Figure 5.5 show that the dynamic pull-in voltage reduces to 0.37 V and 0.29 V when setting the pulse time T equal to 1 ms and 0.1 ms, respectively. As observed by Younis et al. [18] and Askari and Tahani [24], setting the pulse time close to the natural period of the microbeam (T =0.1 ms for the present microsystem) results in dynamic response while higher pulse time (T =1 ms) leads to quasi-steady response. These results are consistent with those reported in [18].

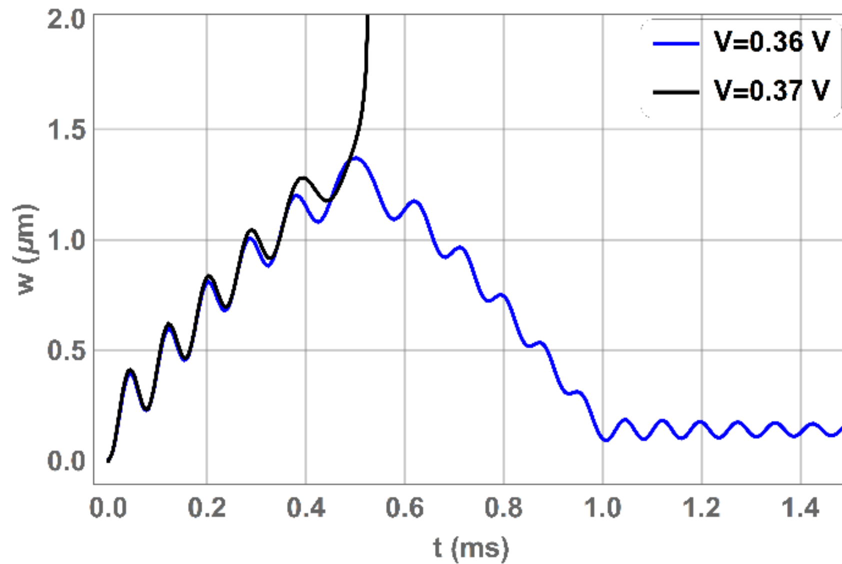

(a)

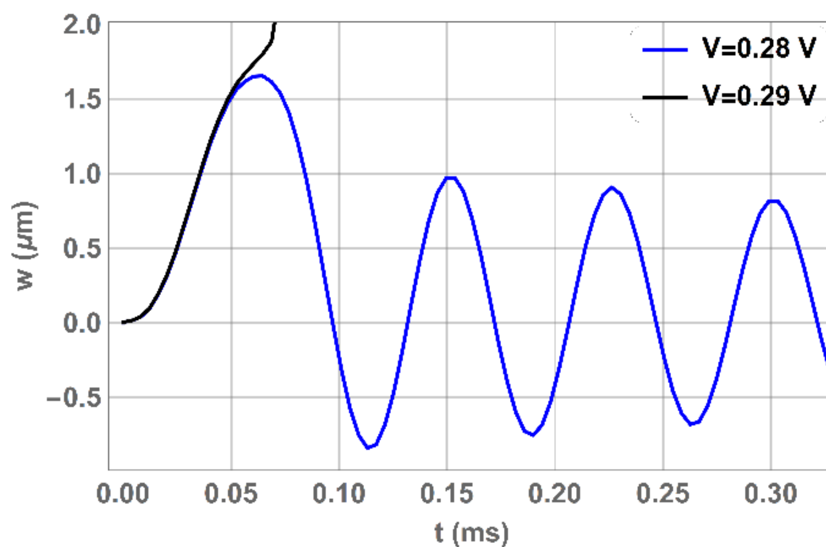

(b)

Figure 5.5: Stable and unstable time history of the microbeam tip: (a) quasi-static (T = 1 ms) and (b) dynamic loading case (T = 0.1 ms).

Next, we incorporate the AC actuation and depict in Figure 5.6 the variations of the dynamic pull-in voltage with the shock amplitude for varying AC voltages (case study 8). The excitation frequency is set equal to 49.5 kHz and the shock pulse time is considered equal to 0.1 ms. for all simulated cases. The dual beam system is found insensitive to mechanical shock up to a critical value. Beyond this value, the dynamic pull-in voltage decreases slightly when increasing the shock amplitude a_0. For instance, a reduction of 25% in the dynamic pull-in voltage is observed when the microsystem is excited with an AC voltage of 0.05 V and undergoes a shock of magnitude 1000 g. As such, the dual beam composed of electrically-actuated microbeams with different geometrical properties can be used for switching applications.

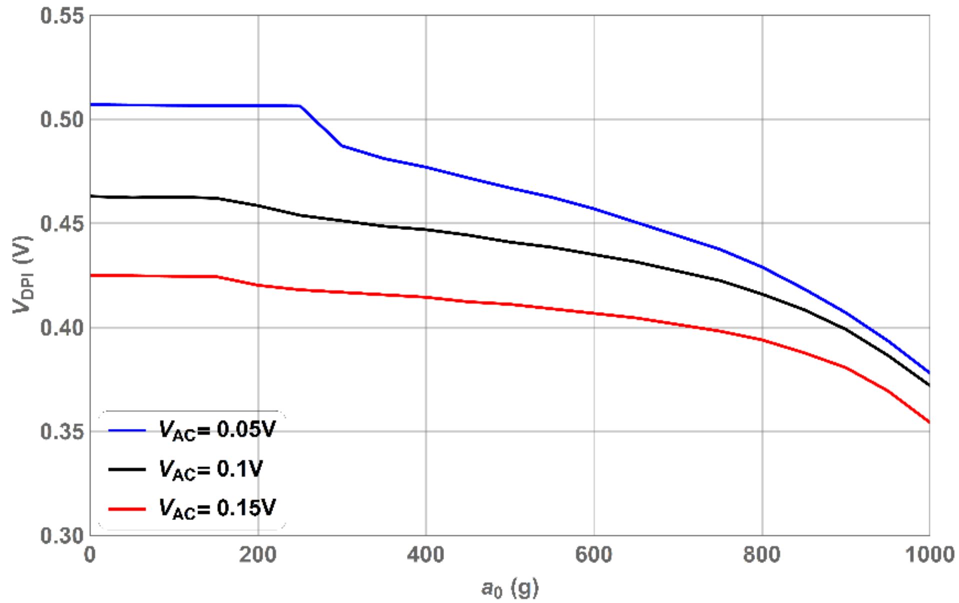

Figure 5.6: Variations of the dynamic pull-in voltage with the amplitude of the mechanical shock for different AC voltages (case study 8).

5.2. Shock Behavior near Resonance

We inspect the dynamic behavior of the microsystem under the mechanical shock when applying an AC voltage with different excitation frequencies. Following Jrad et al. [20], we define the lowest detectable acceleration (LDA) as the minimum shock amplitude required to trigger the pull-in of the microbeam. Figure 5.7 displays the variations of LDA with the DC voltage for different AC voltages while varying the excitation frequency. The obtained results correspond to case study 5 (single beam case). As shown in Figure 5.7 (a), setting the excitation frequency equal to 49.5 kHz

(away from the natural frequency) results in linear decreasing trend in the variations of LDA with the DC voltage V_{DC}. On the other hand, Figure 5.7 (b) shows that operating near the primary resonance (the excitation frequency is set equal to 79.2 kHz) affects significantly the slopes of the LDA-V_{DC} curves and leads to a sudden drop in the LDA values within a range of the DC voltage. This drop shows the weakness of the microstructure being excited within the dynamic pull-in bandwidth for this range of DC voltage. For instance, when applying an AC voltage of 0.05 V we observe the occurrence of a local minimum of the LDA for $V_{DC} = 0:35$ V. Setting the AC voltage equal to 0.1 V results in zero LDA for V_{DC} ranging from 0.3 V to 0.5 V. We notice that the range of the shock amplitudes is not affected by the excitation frequency. For the two cases, it varies between 0 and 800 g. However, it should be noted from Figure 5.7 that the deployment of the electrically-actuated microsystem for switching applications would require less power when activating the AC excitation and selecting the frequency near the primary resonance.

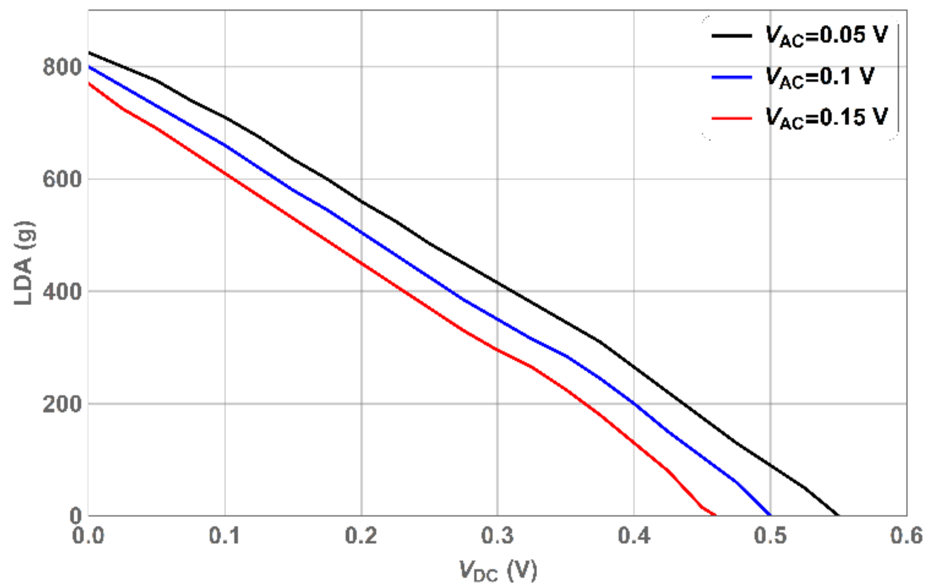

(a)

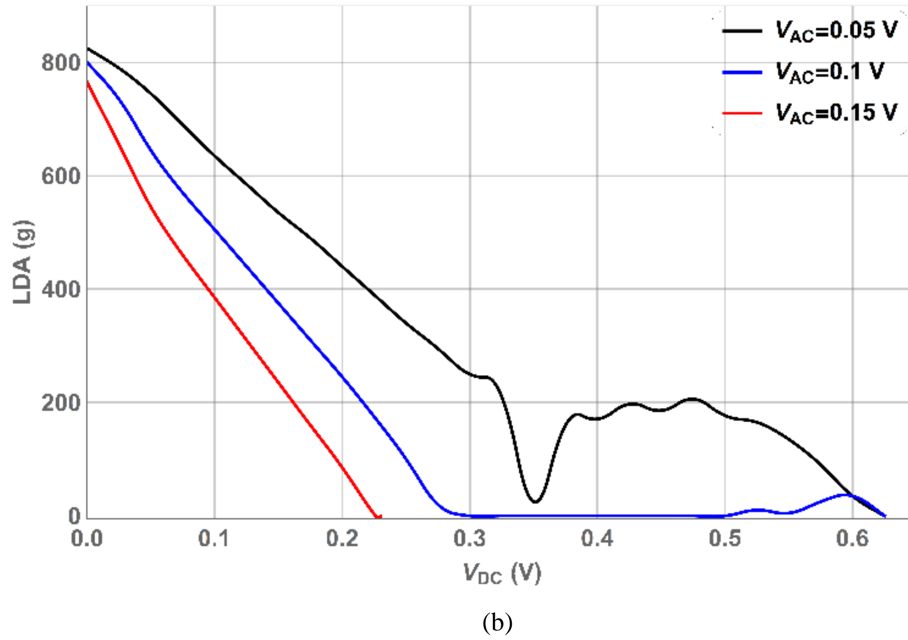

(b)

Figure 5.7: Variations of the lowest detectable acceleration (LDA) with the DC voltage for different AC voltages (case study 5): (a) away from the primary resonance, (b) near the primary resonance.

5.3. Effect of Squeeze-film Damping on Shock Response

It is important to consider the SQFD effect in the design of MEMS devices especially when operating in ambient air. This would depend on the packaging of the MEMS device; that is, the way the vibrating microstructure is capsulated. We show in Figure 5.8 (a), (b), and (c) the time histories of the tip deflection for the single and dual beam system (symmetric and asymmetric configurations), respectively. We recall that the results are shown in terms of the difference between the bending of the two movable microbeams for the dual beam system. For both cases, the microsystem is actuated with a DC voltage and subject to mechanical shock with an amplitude of 400 g and a duration of $T = 1$ ms. Operating in air at ambient pressure level makes the single and dual beams more resistive to mechanical shock. The air between the microbeam and electrode (fixed or movable) suppresses the vibrations. Applying a DC voltage of 0.35V near vacuum conditions results in the collapse of the single beam to the fixed electrode due to the pull-in instability. However, the same voltage value remains safe for the same microsystem when exposing the microbeam to air at ambient pressure conditions. Similar trend is obtained for the asymmetric dual-beam system (different thickness) which shows greater resistance to mechanical shock when operating in air

at ambient conditions. Of interest, the symmetric dual-beam system (identical beams) shows strong resistance to mechanical shock even when actuated with high DC voltage, as the motions of the two beams remain synchronized and in-phase (i.e., the relative distance between them remains constant as illustrated in Figure 5.8 (d) and (e) displaying the absolute tip deflection of each beam separately).

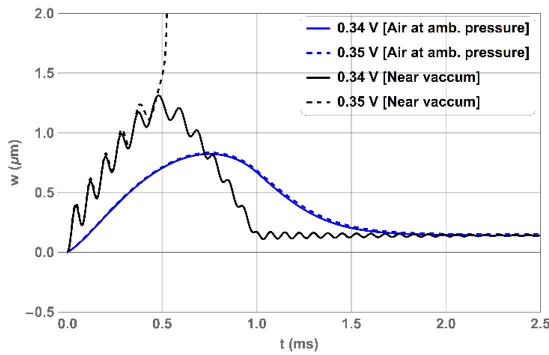

(a) Case study 5 (single beam)

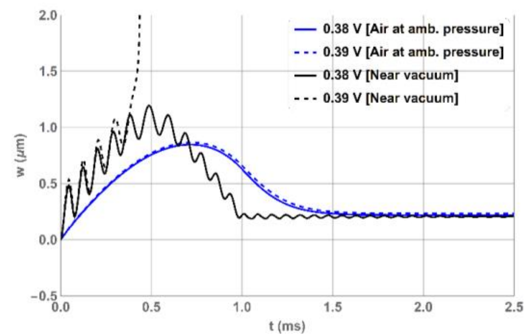

(b) Case study 8 (dual-asymmetric)

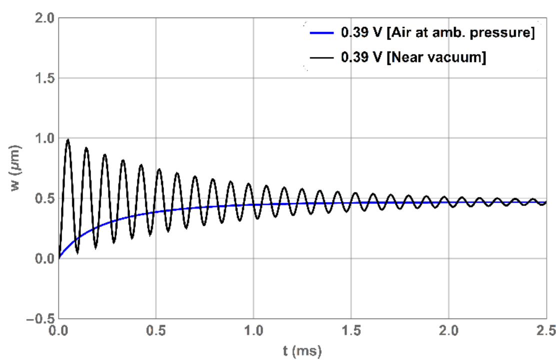

(c) Case study 7 (dual-symmetric)

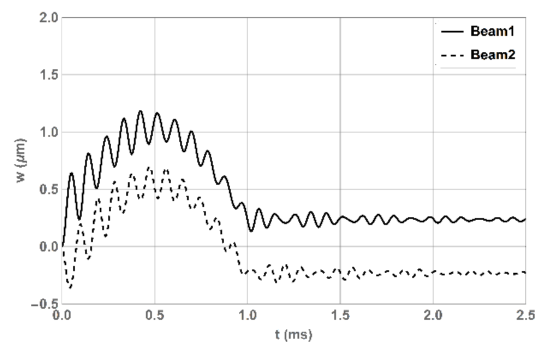

(d) Separate beam analysis in (c) (Near vacuum)

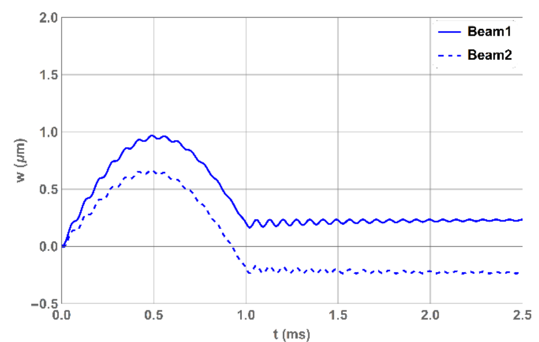

(e) Separate beam analysis in (c) (Air at ambient pressure)

Figure 5.8: Time histories of the single beam's tip deflection under 400g shock amplitude.

Next, we investigate the effect of the pressure on the microstructure under mechanical shock through varying the effective viscosity. We note that the higher the applied pressure is, the larger the viscosity of the surrounding fluid is. We plot in Figure 5.9 the variations of the maximum deflection with the effective viscosity for the single and asymmetric dual beam cases while accounting for the SQFD effect. The simulation results are obtained for varying shock period (pulse time). The applied DC voltage is set equal to $V_{DC} = 0.4$ V and the shock amplitude is maintained at $a_0 = 400$g. The obtained curves show similar trend. At the aforementioned DC voltage and shock level, the microsystem collapses for low values of the viscosity. For instance, when setting the shock period equal to 1 ms, the viscosity of the surrounding fluid (pressurized air) should be higher than 0.002 mPa.s in order to avoid the onset of the pull-in instability. We note that the viscosity is 0.0184 mPa.s at ambient operating conditions. We observe that the maximum deflection decreases as the viscosity is increased and then saturates when reaching high values of the viscosity. Therefore, we may conclude that operating the microstructure under pressurized air (with higher viscosity) is beneficial in many applications to enable stronger protection to mechanical shocks. Of interest, lower values of the tip deflection are obtained when decreasing the shock period. Furthermore, the saturation of the tip deflection tends to occur at lower viscosity values for microbeams under low period shocks. The microbeam shock response is much less dependent on the air viscosity when reaching the value of 0.004 mPa.s for $T = 0.01$ ms. Clearly, the SQFD effect is more significant on the dynamic response of the microbeam which is obtained when the shock period is close to the natural period of the microsystem $T_p = 0.04$ ms. The quasi-static shock response obtained for $T = 1$ ms is less affected by the SQFD. These observations are consistent with the findings reported in [42].

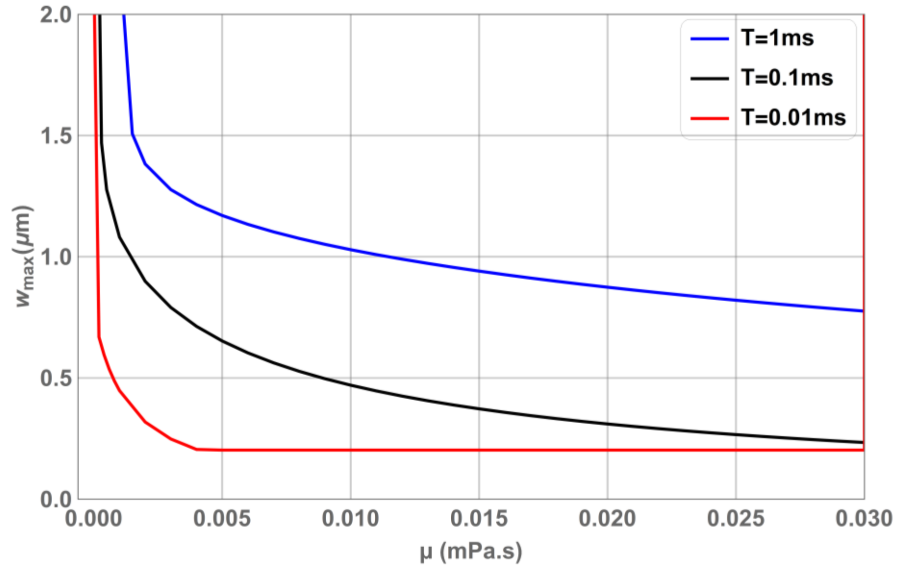

(a) Single beam

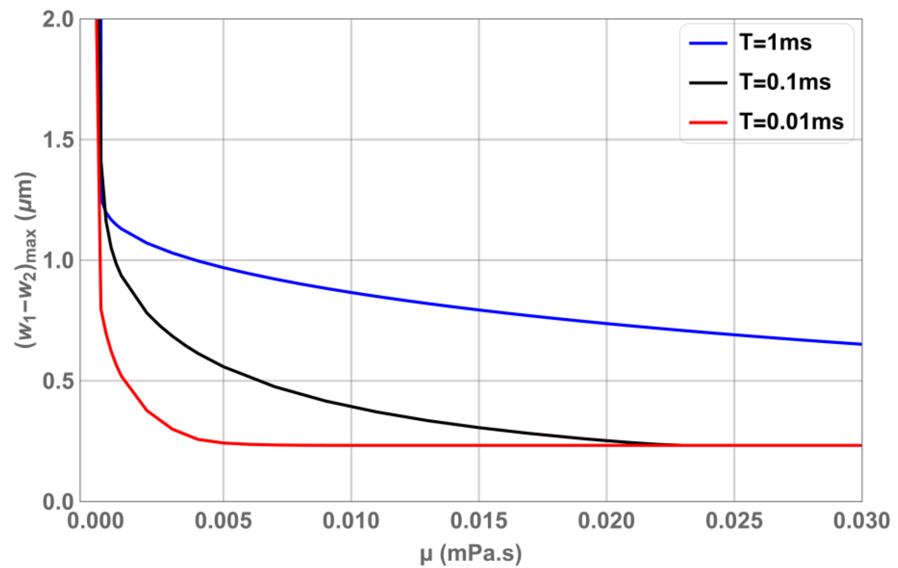

(b) Dual beam (asymmetric)

Figure 5.9: Variations of the maximum tip deflection with the effective viscosity when applying a DC voltage of 0.4V and under 400g shock amplitude. (a) Single beam (b) Dual beam (asymmetric)

The initial gap distance between the two beams (coupled actuation) or the beam and the fixed electrode (uncoupled actuation) is an important design parameter especially when the SQFD effect is considered. We simulate the single beam and dual beam configurations with different gap thicknesses under a shock of amplitude $a_0 =$ 400g and without electrostatic forcing. The objective is to verify qualitatively the shock behavior compared to that reported in the literature [42]. The maximum tip deflection

of the single beam and the maximum relative tip deflection between the two beams in the case of dual beam are computed for varying gap distance denoted by d. The simulation results are displayed in Figure 5.10. The solid curves denote the microbeam shock response obtained when operating in air under ambient conditions. These curves show the occurrence of a critical value of the gap distance leading to maximum tip deflection. Two different regimes of the system behavior are observed. For the range of small gap distances, increasing the value of d yields a decrease in the SQFD force and hence an increase in the tip deflection for a fixed shock load. This trend continues until reaching a critical point where the SQFD effect appears to be negligible and hence, resulting in a decrease in the tip deflection. As the difference in the thickness of the two microbeams is increased, the behavior of the asymmetric dual beam approaches that of the single beam. Referring to Figure 5.10, the dashed lines denote the simulated shock response of the microsystem when operating near vacuum conditions (without accounting for the SQFD force). As expected, these microsystems are observed to be more vulnerable to collapse under the exposure to shock. The maximum tip deflection shows a decreasing trend when increasing the initial gap distance. Again, the dual beam systems (even for the asymmetric configuration) have the capability to withstand more to mechanical shock. The SQDF effect significantly reduces for large gap distances and the shock behavior of the microsystem encapsulated in air (ambient operating conditions) approaches that the near vacuum behavior. For the symmetric dual beam systems, minor change is observed in the shock response when incorporating the SQFD force.

Next, we simulate the dynamic response of the microsystem subjected to 400g shock amplitude under the combined effect of electrostatic force and squeeze-film damping. We consider case study 5 and vary the gap thickness. The results are plotted in Figure 5.11. Clearly, the activation of the electrostatic force causes an abrupt collapse due to dynamic pull-in instability when reaching a critical value of the gap distance given the shock amplitude is maintained fixed. Within the stable range of operation, the curve showing the shock behavior in air still shows the occurrence of an optimal value of the gap distance resulting in the maximum tip deflection. On the other hand, operating near vacuum conditions results in decreasing trend of the tip deflection when shifting the gap distance to higher values.

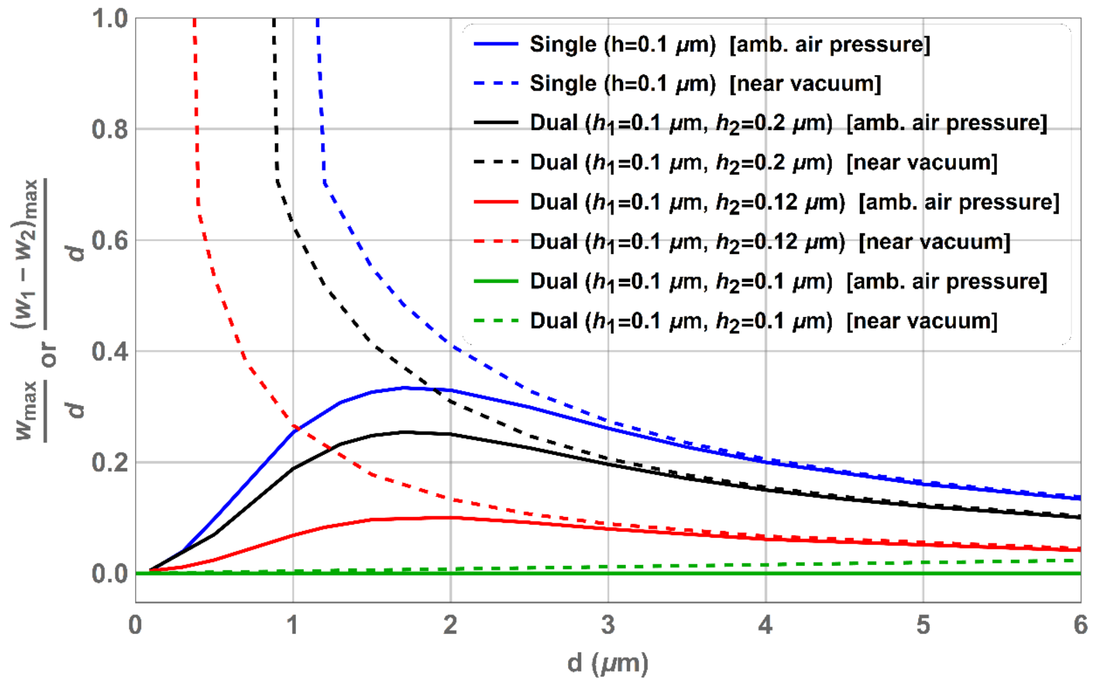

Figure 5.10: Variations of the maximum relative tip deflection of the beams (dual and single beam systems) with the gap distance d under 400g shock amplitude.

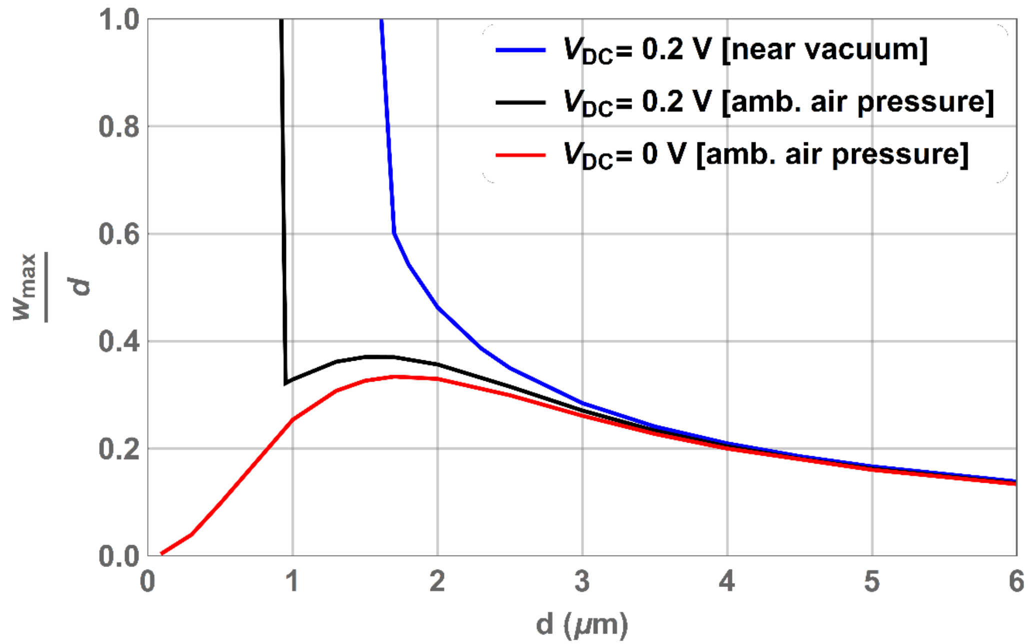

Figure 5.11: Variations of the maximum relative tip deflection of the case study 5 (single beam) with the gap distance d under mechanical shock of amplitude 400g and electrostatic force.

Finally, we generate the least detectable acceleration (LDA) curves to illustrate the potential use of the proposed microsystem designs under different operating conditions for switching applications. We plot in Figure 5.12 the variations of the dynamic pull-in voltage when varying the shock amplitude near vacuum conditions and for air under different pressure levels (ambient and low). We recall that the dynamic pull-in voltage is the critical voltage at which the microbeam collapses under the effect of the shock. The viscosity is set equal to 0.0184 mPa.s and 0.01 mPa.s for the ambient and low pressure conditions, respectively. Results are obtained for the single beam and dual beam systems while varying the shock period. As expected, operating in air induces more resistance to mechanical shock due to the SQFD force for both case studies (see Figure 5.12). The LDA curve is nearly-linear under vacuum condition and a nonlinear trend gradually appears as the pressure increases (the effect of SQFD is more pronounced). The shock period (pulse time) plays an important role in the onset of the dynamic pull-in instability. For near vacuum conditions, setting the shock period equal to 0.1 ms for the single and asymmetric dual beams (close to the system's natural period) leads to amplified dynamics causing an early pull-in. Under the same operating conditions, we observe that increasing the shock period shifts the dynamic pull-in voltage to higher values at fixed shock amplitude. On the other hand, the opposite effect of the shock period is observed when operating in air at different pressure levels. The SQFD effect is more pronounced for shorter shock periods (closer to the natural period of the microsystem).

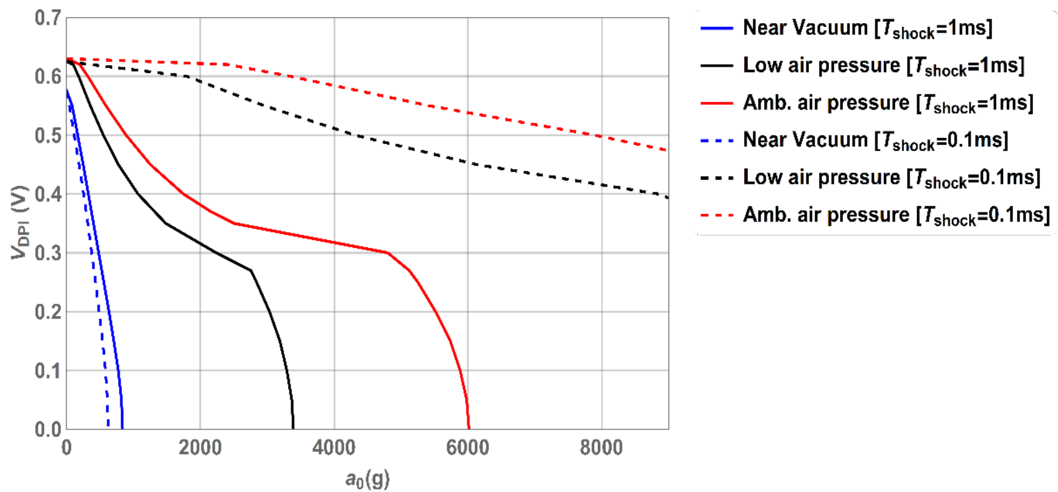

(a) Case study 5 (single beam)

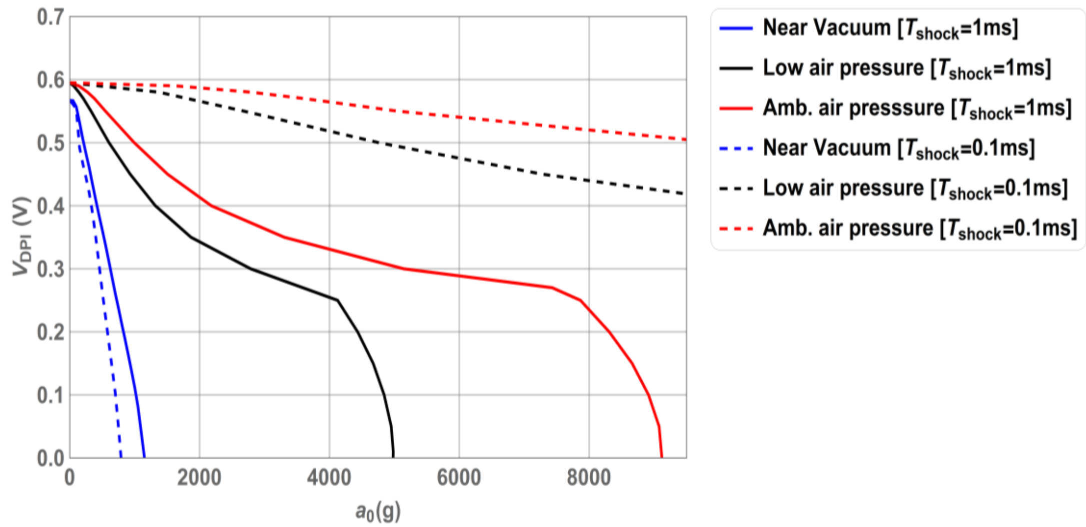

(b) Case study 8 (dual beam - asymmetric)

Figure 5.12: LDA curves for the single and dual beam under different pressure values

The results presented in this section show the possible tunability of the microsystem in terms of geometry (single vs. dual) and microsystem encapsulation (vacuum vs. pressurized air) for switching applications based on the range of shock levels to be detected. This numerical study is also expected to provide guidance to design a robust and reliable microsystem for operation in shock environment.

Chapter 6. Conclusion and Future Work

In this work, we simulated the static and dynamic response of single and dual electrically-actuated microbeams under mechanical shock while considering the effect of Fringing field and squeeze-film damping. The actuation of the single-beam system is made via a fixed electrode (uncoupled actuation) while the dual-beam system, composed of two movable microbeams, is actuated by applying a voltage among them (coupled actuation). The squeeze-film damping was incorporated using a nonlinear analytical expression rather than solving the fully coupled fluid-structure problem. Numerous studies have shown the validity of this analytical approach under the assumption of long beams and neglecting the fluid compressibility. The static analysis of the microsystems showed a significant reduction in the static pull-in voltage and switching time when considering the dual-beam system in comparison with the single-beam case. The Fringing field effect is observed to have a significant impact on the static response when considering narrow microbeams; that is, low width-to-gap distance ratio systems. Furthermore, lower natural frequencies were obtained for electrically-coupled dual beams when compared to those obtained for single beams actuated by a fixed electrode. This indicates the possible use of dual beam resonators when lower operating frequency range is required. The simulation results compared well with those obtained from previously published theoretical and experimental studies. The analysis of the frequency response curves showed expanded dynamic pull-in bandwidth when operating the symmetric dual-beam system near the primary resonance. The present study revealed that the dual-beam systems withstand more to mechanical shock and then they are more suitable for the operation and reliability of MEMS devices in harsh environments characterized by high mechanical shock levels. On the other hand, single-beam systems were found more attractive for use as microswitches which are intended to trigger a signal once receiving a mechanical shock or abrupt change in acceleration to activate safety functionalities such as airbag systems. However, single beams and asymmetric dual beams showed more robustness to operate in shock environment at ambient pressure conditions due to the significant impact of the squeeze-film damping force.

The present numerical study provides insights into the design of the vibrating microstructure in terms of electric actuation (DC and AC excitation), geometry selection (single vs. dual) and encapsulation (vacuum vs. pressurized air) for several MEMS applications. These include switching, sensing, and filtering applications.

As a future work, we plan to proceed with the numerical integration of full nonlinear Reynold's equation coupled with the microbeams governing equations. The results of the full model will be compared against those obtained from the current model. The objective will be to assess further the validity of the analytical approach to model the squeeze film damping and predict the dual beam system behavior near pull-in when operating under ambient conditions.

References

[1] M. I. Younis, *MEMS Linear and Nonlinear Statics and Dynamics*, New York, 2011.

[2] A. Nayfeh and M. I. Younis, "A new approach to the modeling and simulation of flexible microstructures under the effect of squeeze-film damping," *Journal of Micromechanics and Microengineering,* vol. 14, no. 2, pp. 170–181, 2004.

[3] M. Ghommem, A. Nayfeh, S. Choura, F. Najar and E. Abdel-Rahman, "Modeling and performance study of a beam microgyroscope,," *Journal of Sound and Vibration,* vol. 329, no. 23, pp. 4970-4979, 2010.

[4] M. Ghommem, A. Nayfeh and S. Choura, "Model reduction and analysis of a vibrating beam microgyroscope," *Journal of Vibration and Control,* vol. 19, no. 8, pp. 1240–1249, 2013.

[5] M. Ghommem and A. Abdelkefi, "Nonlinear analysis of rotating nanocrystalline silicon microbeams for microgyroscope applications,," *Microsystem Technologies,* vol. 23, no. 12, pp. 5931–5946, 2017.

[6] M. Ghommem and A. Abdelkefi, "Novel design of microgyroscopes employing electrostatic actuation and resistance-change based sensing," *Journal of Sound and Vibration,* vol. 411, pp. 278–288, 2017.

[7] A. Bouchaala, A. H. Nayfeh, N. Jaber and M. Younis, "Mass and position determination in mems mass sensors: a theoretical and an experimental investigation," *Journal of Micromechanics and Microengineering,* vol. 26, no. 10, 2016.

[8] M. Younis and F. Alsaleem, "Exploration of new concepts for mass detection in electrostatically-actuated structures based on nonlinear phenomena," *Journal of Computational and Nonlinear Dynamics,* vol. 4, no. 2, 021010, 2009.

[9] H. R. Akbari, S. Ceballes and A. Abdelkefi, "Geometrical influence of a deposited particle on the performance of bridged carbon nanotube-based mass detectors," *Physica E: Low-dimensional Systems and Nanostructures,* vol. 94, pp. 31-46, 2017.

[10] A. Bouchaala, N. Jaber, O. Yassine, O. Shekhah, V. Chernikova, M. Eddaoudi and M. I. Younis,, "A smart microelectromechanical sensor and switch triggered by gas," *Applied Physics Letters,* vol. 109, no. 1, 013502, 2016.

[11] A. Bouchaala, N. Jaber, O. Yassine, O. Shekhah, V. Chernikova, M. Eddaoudi and M. I. Younis, "Nonlinear-based mems sensors and active switches for gas detection," *Sensors 16,* vol. 16, no. 6, 758, 2016.

[12] A. H. Nayfeh, H. M. Ouakad, F. Najar, S. Choura and E. Abdel-Rahman, "Nonlinear dynamics of a resonant gas sensor," *Nonlinear Dynamics,* vol. 59, no. 4, pp. 607-618, 2010.

[13] H. Ouakad and M. Younis, "On using the dynamic snap-through motion of mems initially curved microbeams for filtering applications," *Journal of Sound and Vibration,* vol. 333, no. 2, pp. 555–568, 2014.

[14] P. Siavash and F. Ayazi, "Electrically coupled mems bandpass filters: partii. without coupling element," *Sensors and Actuators A: Physical,* vol. 122, no. 2, pp. 317–325, 2005.

[15] H. Ouakad and M. Younis, "The dynamic behavior of mems arch resonators actuated electrically," *International Journal of Non-Linear Mechanics,* vol. 45, no. 7, pp. 704–713, 2010.

[16] V. T. Srikar and S. D. Senturia, "The Reliability of Microelectromechanical Systems (MEMS) in Shock Environments," *Journal of Microelectromechanical Systems,* vol. 11, no. 3, pp. 206-214, 2002.

[17] S. Sundaram1, M. Tormen, B. Timotijevic, R. Lockhart, T. Overstolz, R. P. Stanley and H. R. Shea, "Vibration and shock reliability of MEMS: modeling and experimental validation," *Journal of Micromechanics and Microengineering,* vol. 21, no. 4, 045022, 2011.

[18] M. Ibrahim and M. I. Younis,, "The dynamic response of electrostatically driven resonators under mechanical shock," *Journal of Micromechanics and Microengineering,* vol. 20, no. 2, 025006, 2009.

[19] U. Wagner, J. Frank, M. Schweiker, W. Bernhard, R. Muller-Fiedler, B. Michel and O. Paul, "Mechanical reliability of mems-structures under shock load," *Microelectronics Reliability,* vol. 41, no. 9-10, pp. 1657–1662, 2001.

[20] M. Jrad, M. I. Younis and F. Najar, "Modeling and design of an electrically actuated resonant microswitch," *Journal of Vibration and Control,* vol. 22, no. 2, pp. 559–569, 2014.

[21] M. . I. Younis, F. Alsaleem, R. Miles and Q. T. Su, "Characterization of the performance of capacitive switches activated by mechanical shock," *Journal of Micromechanics and Microengineering,* vol. 17, no. 7, pp. 1360-1370, 2007.

[22] M. Younis, F. Alsaleem and D. Jordy, "The response of clamped-clamped microbeams under mechanical shock,," *International Journal of Nonlinear Mechanics,* vol. 42, no. 4, pp. 643-657, 2007.

[23] M. I. Younis, R. Miles and D. Jordy, "Investigation of the response of microstructures under the combined effect of mechanical shock and electrostatic

forces,," *Journal of Micromechanics and Microengineering,* vol. 16, no. 11, pp. 2463–2474, 2006.

[24] A. R. Askari and M. Tahani, "An alternative reduced order model for electrically actuated micro-beams under mechanical shock," *Mechanics Research Communications,* vol. 57, pp. 34-39, 2014.

[25] H. Ouakad, "The response of a micro-electro-mechanical system (MEMS) cantilever-paddle gas sensor to mechanical shock loads," *Journal of Vibration and Control,* vol. 21, no. 14, pp. 2739–2754, 2013.

[26] H. Samaali, F. Najar, S. Choura, A. H. Nayfeh and M. Masmoudi, "A double microbeam mems ohmic switch for rf-applications with low actuation voltage," *Nonlinear Dynamics,* vol. 63, no. 4, pp. 719–734, 2011.

[27] H. Samaali, F. Najar and S. Choura, "Dynamic Study of a Capacitive MEMS Switch with Double Clamped-Clamped Microbeams," *Shock and Vibration,* vol. 2014, 2014.

[28] A. Ramini, M. I. Younis and Q. T Su, "Low-G Electrostatically Actuated Resonant Switch," *Smart Materials and Structures,* vol. 22, no. 2, 025006, 2013.

[29] H. Dai and L. Wang, "Surface effect on the pull-in instability of cantilevered nano-switches based on a full nonlinear model," *Physica E,* vol. 73, pp. 141-147, 2015.

[30] T. Gordon Brown,, B. Davis, D. Hepner, J. Faust, C. Myers, P. Muller, T. Harkins, M. Hollis, C. Miller and B. Placzankis, "Strap-Down Microelectromechanical (MEMS) Sensors for High-G Munition Applications," *IEEE Transactions on Magnetics,* vol. 37, no. 1, pp. 336-342, 2001.

[31] D. Parkos, N. Raghunathan, A. Venkattraman, B. Sanborn, W. Chen and D. Peroulis, "Near-contact gas damping and dynamic response of high-g mems accelerometer beams," *Journal of Microelectromechanical Systems,* vol. 22, no. 5, pp. 1089–1099, 2013.

[32] N. Raghunathan, E. Fruehling, W. Cheny and D. Peroulis, "Arrays of silicon cantilevers for detecting high-g rapidly varying acceleration profiles,," *IEEE SENSORS 2010 Conference,* pp. 1203–1206, 2010.

[33] H. M. Ouakad and J. E. AlQasimi, "Reliability of MEMS shallow arches based actuator under the combined effect of mechanical shock and electric loads," *Microelectronics Reliability,* vol. 79, pp. 352–359, 2017.

[34] S. Ilyas, K. N. Chappanda, M. A. Al Hafiz, A. Ramini and M. I. Younis, "An experimental and theoretical investigation of electrostatically coupled cantilever microbeams," *Sensors and Actiators A: Physical,* vol. 247, pp. 368-378, 2016.

[35] M. Napoli, Z. Wenhua, K. Turner and B. Bassam, "Characterization of Electrostatically Coupled Microcantilevers," *Journal of Microelectromechanical Systems,* vol. 14, no. 2, pp. 295-304, 2005.

[36] J. B. Starr, "Squeeze-film damping in solid-state accelerometers," *in Proceeding of the IEEE Solid-State Sensor and Actuator Workshop,* pp. 44–47, 1990.

[37] J. J. Blech, "On Isothermal Squeeze Films," *Journal of Lubrication Technology,* vol. 105, no. 4, pp. 615-620, 1983.

[38] P. Li, H. Rufu and Y. Fang, "A new model for squeeze-film damping of electrically actuated microbeams under the effect of a static deflection," *Journal of Micromechanics and Microengineering,* vol. 17, no. 7, pp. 1242–1251, 2007.

[39] I. Hosseini, M. Moghimi Zand and M. Lotfi, "Dynamic pull-in and snap-through behavior in micro/nano mechanical memories considering squeeze film damping," *Microsystem Technologies,* vol. 23, no. 5, pp. 1423–1432, 2017.

[40] D. Jordy and M. I. Younis, "Characterization of the Dynamical Response of a Micromachined G-Sensor to Mechanical Shock Loading," *Journal of Dynamic Systems, Measurement, and Control,* vol. 1, pp. 913-921, 2008.

[41] F. M. Alsaleem, M. I. Younis and M. I. Ibrahim, "A Study for the Effect of the PCB Motion on the Dynamics of MEMS Devices Under Mechanical Shock," *Journal of Microelectromechanical Systems,* vol. 18, no. 3, pp. 597-609, 2009.

[42] H. Yagubizade and M. I. Younis, "The Effect of Squeeze-Film Damping on the Shock Response of Clamped-Clamped Microbeams," *Journal of Dynamic Systems, Measurement, and Control,* vol. 134, no. 1, 011017, 2012.

[43] J. Abderezaei and M. Moghimi Zand, "Transient behavior of electrostatically actuated micro systems considering squeeze film damping and mechanical shock," *Scientia Iranica,* vol. 24, no. 4, pp. 2887-2894, 2017.

[44] R. C. Batra, M. Porfiri and D. Spinello, "Capacitance estimate for electrostatically actuated narrow microbeams," *Micro & Nano Letters,* vol. 1, no. 2, pp. 71-73, 2007.

[45] R. Batra, M. Porfiri and D. Spinello, "Electromechanical Model of Electrically Actuated Narrow Microbeams," *Journal of Microelectromechanical Systems,* vol. 15, no. 5, pp. 1175 - 1189, 2006.

[46] H. Ouakad, "Static Response and Natural Frequencies of Microbeams Actuated by Out-of-Plane Electrostatic Fringing-Fields," *International Journal of Non-Linear Mechanics,* vol. 63, pp. 39-48, 2014.

[47] J. W. Lee, R. Tung, A. Raman, H. Sumali and J. P. Sullivan, "Squeeze-film damping of flexible microcantilevers at low ambient pressures: theory and

experiment," *Journal of Micromechanics and Microengineering,* vol. 19, no. 10, 105029, 2009.

[48] B. Mohammadi-Alasti, G. Rezazadeh, A.-M. Borgheei, S. Minaei and R. Habibifar, "On the mechanical behavior of a functionally graded micro-beam subjected to a thermal moment and nonlinear electrostatic pressure," *Composite Structures,* vol. 93, no. 6, pp. 1516–1525, 2010.

[49] M. SoltanRezaee and M. Afrashi, "Modeling the nonlinear pull-in behavior of tunable nano-switches," *International Journal of Engineering Science,* vol. 109, pp. 73-87, 2016.

[50] H. Ouakad, "Electrostatic fringing-fields effects on the structural behavior of MEMS shallow arches," *Microsystem Technologies,* vol. 24, no. 3, pp. 1391-1399, 2016.

Vita

Moustafa Sayed Ahmed was born in 1993, in Dubai, United Arab Emirates. He received his primary and secondary education in Dubai, UAE. He received his B.Sc. degree in Mechanical Engineering from the American University of Sharjah in June 2016. In September 2016, he joined the Mechanical Engineering master's program at the American University of Sharjah as a graduate teaching assistant. His research interest is in the nonlinear dynamics for MEMS applications.